

---

# Lost in Latent Space: An Empirical Study of Latent Diffusion Models for Physics Emulation

---

François Rozet<sup>1,2,3</sup> Ruben Ohana<sup>1,2</sup> Michael McCabe<sup>1,4</sup>  
 Gilles Louppe<sup>3</sup> François Lanusse<sup>1,2,6</sup> Shirley Ho<sup>1,2,4,5</sup>

<sup>1</sup>Polymathic AI <sup>2</sup>Flatiron Institute <sup>3</sup>University of Liège  
<sup>4</sup>New York University <sup>5</sup>Princeton University  
<sup>6</sup>Université Paris-Saclay, Université Paris Cité, CEA, CNRS, AIM

## Abstract

The steep computational cost of diffusion models at inference hinders their use as fast physics emulators. In the context of image and video generation, this computational drawback has been addressed by generating in the latent space of an autoencoder instead of the pixel space. In this work, we investigate whether a similar strategy can be effectively applied to the emulation of dynamical systems and at what cost. We find that the accuracy of latent-space emulation is surprisingly robust to a wide range of compression rates (up to 1000 $\times$ ). We also show that diffusion-based emulators are consistently more accurate than non-generative counterparts and compensate for uncertainty in their predictions with greater diversity. Finally, we cover practical design choices, spanning from architectures to optimizers, that we found critical to train latent-space emulators.

## 1 Introduction

Numerical simulations of dynamical systems are at the core of many scientific and engineering disciplines. Solving partial differential equations (PDEs) that describe the dynamics of physical phenomena enables, among others, weather forecasts [1, 2], predictions of solar wind and flares [3–5], or control of plasma in fusion reactors [6, 7]. These simulations typically operate on fine-grained spatial and temporal grids and require significant computational resources for high-fidelity results.

To address this limitation, a promising strategy is to develop neural network-based emulators to make predictions orders of magnitude faster than traditional numerical solvers. The typical approach [8–17] is to consider the dynamics as a function  $f(x^i) = x^{i+1}$  that evolves the state  $x^i$  of the system and to train a neural network  $f_\phi(x)$  to approximate that function. In the context of PDEs, this network is sometimes called a neural solver [11, 18, 19]. After training, the autoregressive application of the solver, or rollout, emulates the dynamics. However, recent studies [11, 18–21] reveal that, while neural solvers demonstrate impressive accuracy for short-term prediction, errors accumulate over the course of the rollout, leading to distribution shifts between training and inference. This phenomenon is even more severe for stochastic or undetermined systems, where it is not possible to predict the next state given the previous one(s) with certainty. Instead of modeling the uncertainty, neural solvers produce a single point estimate, usually the mean, instead of a distribution.

The natural choice to alleviate these issues are generative models, in particular diffusion models, which have shown remarkable results in recent years. Following their success, diffusion models have been applied to emulation tasks [18, 19, 22–25] for which they were found to mitigate the rollout instability of non-generative emulators. However, diffusion models are much more expensive than deterministic alternatives at inference, due to their iterative sampling process, which defeats the purpose of using an emulator. To address this computational drawback, many works in the image and

video generation literature [26–32] consider generating in the latent space of an autoencoder. This approach has been adapted with success to the problem of emulating dynamical systems [33–37], sometimes even outperforming pixel-space emulation. In this work, we seek to answer a simple question: *What is the impact of latent-space compression on emulation accuracy?* To this end, we train and systematically evaluate latent-space emulators across a wide range of compression rates for challenging dynamical systems from TheWell [38]. Our results indicate that

- i. Latent diffusion-based emulation is surprisingly robust to the compression rate, even when autoencoder reconstruction quality greatly degrades.
- ii. Latent-space emulators match or exceed the accuracy of pixel-space emulators, while using fewer parameters and less training compute.
- iii. Diffusion-based emulators consistently outperform their non-generative counterparts in both accuracy and plausibility of the emulated dynamics.

Finally, we dedicate part of this manuscript to design choices. We discuss architectural and modeling decisions for autoencoders and diffusion models that enable stable training of latent-space emulators under high compression. To encourage further research in this direction, we provide the code for all experiments at <https://github.com/polymathicai/lola> along with pre-trained model weights.

## 2 Diffusion models

The primary purpose of diffusion models (DMs) [39, 40], also known as score-based generative models [41, 42], is to generate plausible data from a distribution  $p(x)$  of interest. Formally, continuous-time diffusion models define a series of increasingly noisy distributions

$$p(x_t) = \int p(x_t | x) p(x) dx = \int \mathcal{N}(x_t | \alpha_t x, \sigma_t^2 I) p(x) dx \quad (1)$$

such that the ratio  $\alpha_t/\sigma_t \in \mathbb{R}_+$  is monotonically decreasing with the time  $t \in [0, 1]$ . For such a series, there exists a family of reverse-time stochastic differential equations (SDEs) [42–44]

$$dx_t = \left[ f_t x_t - \frac{1 + \eta^2}{2} g_t^2 \nabla_{x_t} \log p(x_t) \right] dt + \eta g_t dw_t \quad (2)$$

where  $\eta \geq 0$  is a parameter controlling stochasticity, the coefficients  $f_t$  and  $g_t$  are derived from  $\alpha_t$  and  $\sigma_t$  [42–44], and for which the variable  $x_t$  follows  $p(x_t)$ . In other words, we can draw noise samples  $x_1 \sim p(x_1) \approx \mathcal{N}(0, \sigma_1^2 I)$  and obtain data samples  $x_0 \sim p(x_0) \approx p(x)$  by solving Eq. (2) from  $t = 1$  to  $0$ . For high-dimensional samples, the terminal signal-to-noise ratio  $\alpha_1/\sigma_1$  should be at or very close to zero [45]. In this work, we adopt the rectified flow [28, 46, 47] noise schedule, for which  $\alpha_t = 1 - t$  and  $\sigma_t = t$ .

**Denoising score matching** In practice, the score function  $\nabla_{x_t} \log p(x_t)$  in Eq. (2) is unknown, but can be approximated by a neural network trained via denoising score matching [48, 49]. Several equivalent parameterizations and objectives have been proposed for this task [40–42, 47, 50, 51]. In this work, we adopt the denoiser parameterization  $d_\phi(x_t, t)$  and its objective [51]

$$\arg \min_{\phi} \mathbb{E}_{p(x)p(t)p(x_t|x)} \left[ \lambda_t \|d_\phi(x_t, t) - x\|_2^2 \right], \quad (3)$$

for which the optimal denoiser is the mean  $\mathbb{E}[x | x_t]$  of  $p(x | x_t)$ . Importantly,  $\mathbb{E}[x | x_t]$  is linked to the score function through Tweedie's formula [52–55]

$$\mathbb{E}[x | x_t] = \frac{x_t + \sigma_t^2 \nabla_{x_t} \log p(x_t)}{\alpha_t}, \quad (4)$$

which allows to use  $s_\phi(x_t) = \sigma_t^{-2} (d_\phi(x_t, t) - \alpha_t x_t)$  as a score estimate in Eq. (2).

## 3 Methodology

In this section, we detail and motivate our experimental methodology for investigating the impact of compression on the accuracy of latent-space emulators. To summarize, we consider three challenging

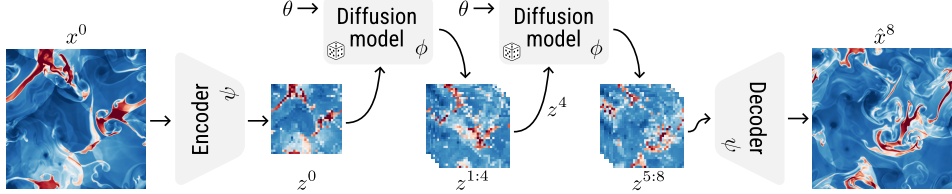


Figure 1. Illustration of the latent-space emulation process. At each step of the autoregressive rollout, the diffusion model generates the next  $n = 4$  latent states  $z^{i+1:i+n}$  given the current state  $z^i$  and the simulation parameters  $\theta$ . After rollout, the generated latent states are decoded to pixel space.

datasets from TheWell [38]. For each dataset, we first train a series of autoencoders with varying compression rates. These autoencoders learn to map high-dimensional physical states  $x^i \in \mathbb{R}^{H \times W \times C_{\text{pixel}}}$  to low-dimensional latent representations  $z^i \in \mathbb{R}^{\frac{H}{r} \times \frac{W}{r} \times C_{\text{latent}}}$ . Subsequently, for each autoencoder, we train two emulators operating in the latent space: a diffusion model (generative) and a neural solver (non-generative). Both are trained to predict the next  $n$  latent states  $z^{i+1:i+n}$  given the current latent state  $z^i$  and simulation parameters  $\theta$ . This technique, known as temporal bundling [11], mitigates the accumulation of errors during rollout by decreasing the number of required autoregressive steps. After training, latent-space emulators are used to produce autoregressive rollouts  $z^{1:L}$  starting from known initial state  $z^0 = E_\psi(x^0)$  and simulation parameters  $\theta$ , which are then decoded to the pixel space as  $\hat{x}^i = D_\psi(z^i)$ .

### 3.1 Datasets

To study the effects of extreme compression rates, the datasets we consider should be high-dimensional and contain large amounts of data. Intuitively, the effective size of the dataset decreases in latent space, making overfitting more likely at fixed model capacity. According to these criteria, we select three datasets from TheWell [38]. Additional details are provided in Appendix B.

**Euler Multi-Quadrants** The Euler equations model the behavior of compressible non-viscous fluids. In this dataset, the initial state presents multiple discontinuities which result in interacting shock waves as the system evolves for 100 steps. The 2d state of the system is represented with three scalar fields (energy, density, pressure) and one vector field (momentum) discretized on a  $512 \times 512$  grid, for a total of  $C_{\text{pixel}} = 5$  channels. Each simulation has either periodic or open boundary conditions and a different heat capacity  $\gamma$ , which constitutes their parameters  $\theta$ . We set a time stride  $\Delta = 4$  between consecutive states  $x^i$  and  $x^{i+1}$ , such that the simulation time  $\tau = i \times \Delta$ .

**Rayleigh-Bénard (RB)** The Rayleigh-Bénard convection phenomenon occurs when an horizontal layer of fluid is heated from below and cooled from above. Over the 200 simulation steps, the temperature difference leads to the formation of convection currents where cooler fluid sinks and warmer fluid rises. The 2d state of the system is represented with two scalar fields (buoyancy, pressure) and one vector field (velocity) discretized on a  $512 \times 128$  grid, for a total of  $C_{\text{pixel}} = 4$  channels. Each simulation has different Rayleigh and Prandtl numbers as parameters  $\theta$ . We set a time stride  $\Delta = 1$ .

**Turbulence Gravity Cooling (TGC)** The interstellar medium can be modeled as a turbulent fluid subject to gravity and radiative cooling. Starting from an homogeneous state, dense filaments form in the fluid, leading to the birth of stars. The 3d state of the system is represented with three scalar fields (density, pressure, temperature) and one vector field (velocity) discretized on a  $64 \times 64 \times 64$  grid, for a total of  $C_{\text{pixel}} = 6$  channels. Each simulation has different initial conditions function of their density, temperature, and metallicity. We set a time stride  $\Delta = 1$ .

### 3.2 Autoencoders

To isolate the effect of compression, we use a consistent autoencoder architecture and training setup across datasets and compression rates. We focus on compressing individual states  $x^i$  into latent states  $z^i = E_\psi(x^i)$ , which are reconstructed as  $\hat{x}^i = D_\psi(z^i)$ .

**Architecture** We adopt a convolution-based autoencoder architecture similar to the one used by Rombach et al. [26], which we adapt to perform well under high compression rates. Specifically, inspired by Chen et al. [31], we initialize the downsampling and upsampling layers near identity, which enables training deeper architectures with complex latent representations, while preserving reconstruction quality. For 2d datasets (Euler and RB), we set the spatial downsampling factor  $r = 32$  for all autoencoders, meaning that a  $32 \times 32$  patch in pixel space corresponds to one token in latent space. For 3d datasets (TGC), we set  $r = 8$ . The compression rate is then controlled solely by varying the number of channels per token in the latent representation. For instance, with the Euler dataset, an autoencoder with  $C_{\text{latent}} = 64$  latent channels – f32c64 in the notations of Chen et al. [31] – transforms the input state with shape  $512 \times 512 \times 5$  to a latent state with shape  $16 \times 16 \times 64$ , yielding a compression rate of 80. This setup ensures that the architectural capacity remains similar for all autoencoders and allows for fair comparison across compression rates. Further details as well as a short ablation study are provided in Appendix B.

**Training** Latent diffusion models [26] often rely on a Kullback-Leibler (KL) divergence penalty to encourage latents to follow a standard Gaussian distribution. However, this term is typically down-weighted by several orders of magnitude to prevent severe reconstruction degradation. As such, the KL penalty acts more as a weak regularization than a proper variational objective [56] and post-hoc standardization of latents is often necessary. We replace this KL penalty with a deterministic saturating function

$$z \mapsto \frac{z}{\sqrt{1 + z^2/B^2}} \quad (5)$$

applied to the encoder’s output. In our experiments, we choose the bound  $B = 5$  to mimic the range of a standard Gaussian distribution. We find this approach simpler and more effective at structuring the latent space, without introducing a tradeoff between regularization and reconstruction quality. We additionally omit perceptual [57] and adversarial [58, 59] loss terms, as they are designed for natural images where human perception is the primary target, unlike physics. The training objective thus simplifies to a reconstruction loss

$$\arg \min_{\psi} \mathbb{E}_{p(x)} [\ell(x, D_{\psi}(E_{\psi}(x)))]. \quad (6)$$

The loss  $\ell$  is typically a variation of  $L_1$  or  $L_2$  regression, which we discuss in Appendix B. Finally, we find that preconditioned optimizers [60–62] greatly accelerate the training convergence of autoencoders compared to the widespread Adam [63] optimizer (see Table 4). We adopt the PSGD [60] implementation in the heavyball [64] library for its fewer number of tunable hyper-parameters and lower memory footprint than SOAP [62].

### 3.3 Diffusion models

We train diffusion models to predict the next  $n$  latent states  $z^{i+1:i+n}$  given the current state  $z^i$  and simulation parameters  $\theta$ , that is to generate from  $p(z^{i+1:i+n} | z^i, \theta)$ . We parameterize our diffusion models with a denoiser  $d_{\phi}(z_t^{i:i+n}, b, \theta, t)$  whose task is to denoise sequences of noisy states  $z_t^i \sim p(z_t^i | z^i) = \mathcal{N}(z_t^i | \alpha_t z^i, \sigma_t^2 I)$  given the parameters  $\theta$  of the simulation. Conditioning with respect to known elements in the sequence  $z^{i:i+n}$  is tackled with a binary mask  $b \in \{0, 1\}^{n+1}$  concatenated to the input, as in MCVD [65]. For instance,  $b = (1, 0, \dots, 0)$  indicates that the first element  $z^i$  is known, while  $b = (1, \dots, 1, 0)$  indicates that the first  $n - 1$  elements  $z^{i:i+n-1}$  are known. Known elements are provided to the denoiser without noise.

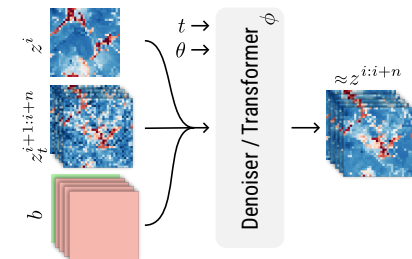


Figure 2. Illustration of the denoiser’s inputs and outputs, while generating from  $p(z^{i+1:i+n} | z^i, \theta)$ .

**Architecture** Drawing inspiration from recent successes in latent image generation [27–31], we use a transformer-based architecture for the denoiser. We incorporate several architectural refinements shown to improve performance and stability, including query-key normalization [66], rotary positional embedding (RoPE) [67, 68], and value residual learning [69]. The transformer operates on the spatial and temporal axes of the input  $z_t^{i:i+n}$ , while the parameters  $\theta$  and diffusion time  $t$  modulate the

transformer blocks. Thanks to the considerable ( $r = 32$ ) spatial downsampling performed by the autoencoder, we are able to apply full spatio-temporal attention, avoiding the need for sparse attention patterns [70–72]. Finally, we fix the token embedding size (1024) and the number of transformer blocks (16) for all diffusion models. The only architectural variation stems from the number of input and output channels dictated by the corresponding autoencoder.

**Training** As in Section 2, diffusion models are trained via denoising score matching [48, 49]

$$\arg \min_{\phi} \mathbb{E}_{p(\theta, z^{i:i+n}, z_t^{i:i+n})p(b)} \left[ \left\| d_{\phi} \left( \underbrace{z^{i:i+n}}_{\text{clean}} \odot b + \underbrace{z_t^{i:i+n}}_{\text{noisy}} \odot (1-b), b, \theta, t \right) - z^{i:i+n} \right\|_2^2 \right] \quad (7)$$

with the exception that the data does not come from the pixel-space distribution  $p(\theta, x^{1:L})$  but from the latent-space distribution  $p(\theta, z^{1:L})$  determined by the encoder  $E_{\psi}$ . Following Voleti et al. [65], we randomly sample the binary mask  $b \sim p(b)$  during training to cover several conditioning tasks, including prediction with variable-length context  $p(z^{i+c:i+n} | z^{i:i+c-1})$ .

**Sampling** After training, we sample from the learned distribution by solving Eq. (2) with  $\eta = 0$ , which corresponds to the probability flow ODE [42]. To this end, we implement a 3rd order Adams-Basforth multi-step integration method, as proposed by Zhang et al. [73]. Intuitively, this method leverages information from previous integration steps to improve accuracy. We find this approach highly effective, producing high-quality samples with significantly fewer neural function evaluations (NFEs) than other widespread samplers [50, 51].

### 3.4 Neural solvers

We train neural solvers to perform the same task as diffusion models. Unlike the latter, however, solvers do not generate from  $p(z^{i+1:i+n} | z^i, \theta)$ , but produce a point estimate  $f_{\phi}(z_i, \theta) \approx \mathbb{E}[z^{i+1:i+n} | z_i, \theta]$  instead. We also train a pixel-space neural solver, for which  $z^i = x^i$ , as baseline.

**Architecture** For latent-space neural solvers, we use the same transformer-based architecture as for diffusion models. The only notable difference is that transformer blocks are only modulated with respect to the simulation parameters  $\theta$ . For the pixel-space neural solver, we keep the same architecture, but group the pixels into  $16 \times 16$  patches, as in vision transformers [74]. We also double the token embedding size (2048) such that the pixel-space neural solver has roughly two times more trainable parameters than an autoencoder and latent-space emulator combined.

**Training** Neural solvers are trained via mean regression

$$\arg \min_{\phi} \mathbb{E}_{p(\theta, z^{i:i+n})p(b)} \left[ \left\| f_{\phi}(z^{i:i+n} \odot b, b, \theta) - z^{i:i+n} \right\|_2^2 \right]. \quad (8)$$

Apart from the training objective, the training configuration (optimizer, learning rate schedule, batch size, epochs, masking, ...) for neural solvers is strictly the same as for diffusion models.

### 3.5 Evaluation metrics

We consider several metrics for evaluation, each serving a different purpose. We report these metrics either at a lead time  $\tau = i \times \Delta$  or averaged over a lead time horizon  $a:b$ . If the states  $x^i$  present several fields, the metric is first computed on each field separately, then averaged.

**Variance-normalized RMSE** The root mean squared error (RMSE) and its normalized variants are widespread metrics to quantify the point-wise accuracy of an emulation [21, 38, 75]. Following Ohana et al. [38], we pick the variance-normalized RMSE (VRMSE) over the more common normalized RMSE (NRMSE), as the latter down-weights errors in non-negative fields such as pressure and density. Formally, for two spatial fields  $u$  and  $v$ , the VRMSE is defined as

$$\text{VRMSE}(u, v) = \sqrt{\frac{\langle (u - v)^2 \rangle}{\langle (u - \langle u \rangle)^2 \rangle + \epsilon}} \quad (9)$$

where  $\langle \cdot \rangle$  denotes the spatial mean operator and  $\epsilon = 10^{-6}$  is a numerical stability term.

**Power spectrum RMSE** For chaotic systems such as turbulent fluids, it is typically intractable to achieve accurate long-term emulation as very small errors can lead to entirely different trajectories later on. In this case, instead of reproducing the exact trajectory, emulators should generate diverse trajectories that remain statistically plausible. Intuitively, even though structures are wrongly located, the types of patterns and their distribution should stay similar [76]. Following Ohana et al. [38], we assess statistical plausibility by comparing the power spectra of the ground-truth and emulated trajectories. For two spatial fields  $u$  and  $v$ , we compute the isotropic power spectra  $p_u$  and  $p_v$  and split them into three frequency bands (low, mid and high) evenly distributed in log-space. We report the RMSE of the relative power spectra  $p_v/p_u$  over each band.

**Spread-skill ratio** In earth sciences [25, 75], the skill of an ensemble of  $K$  particles is defined as the RMSE of the ensemble mean. The spread is defined as the ensemble standard deviation. Under these definitions and the assumption of a perfect forecast where ensemble particles are exchangeable, Fortin et al. [75] show that

$$\text{Skill} \approx \sqrt{K+1/K} \text{ Spread} . \quad (10)$$

This motivates the use of the (corrected) spread-skill ratio as a metric. Intuitively, if the ratio is smaller than one, the ensemble is biased or under-dispersed. If the ratio is larger than one, the ensemble is over-dispersed. It should be noted, however, that a spread-skill ratio of 1 is a necessary but insufficient condition for a perfect forecast.

## 4 Results

We start with the evaluation of the autoencoders. For all datasets, we train three autoencoders with respectively 64, 16, and 4 latent channels. These correspond to compression rates of 80, 320 and 1280 for the Euler dataset, 64, 256, and 1024 for the RB dataset, and 48, 192, 768 for the TGC dataset, respectively. In the following, we refer to models by their compression rate. Additional experimental details are provided in Section 3 and Appendix B.

For each autoencoder, we evaluate the reconstruction  $\hat{x}^i = D_\psi(E_\psi(x^i))$  of all states  $x^i$  in 64 test trajectories  $x^{0:L}$ . As expected, when the compression rate increases, the reconstruction quality degrades, as reported in Figure 3. For the Euler dataset, the reconstruction error grows with the lead time due to wavefront interactions and rising high-frequency content. For the RB dataset, the reconstruction error peaks mid-simulation during the transition from low to high-turbulence regime. Similar trends can be observed for the power spectrum RMSE in Tables 8, 9 and 10, where the high-frequency band is most affected by compression. These results so far align with what practitioners intuitively expect from lossy compression.

We now turn to the evaluation of the emulators. For each autoencoder, we train two latent-space emulators: a diffusion model and a neural solver. Starting from the initial state  $z^0 = E_\psi(x^0)$  and simulation parameters  $\theta$  of 64 test trajectories  $x^{0:L}$ , each emulator produces 16 distinct autoregressive rollouts  $z^{1:L}$ , which are then decoded to the pixel space as  $\hat{x}^i = D_\psi(z^i)$ . Note that for neural solvers, all 16 rollouts are identical. We compute the metrics of each prediction  $\hat{x}^i$  against the ground-truth state  $x^i$ .

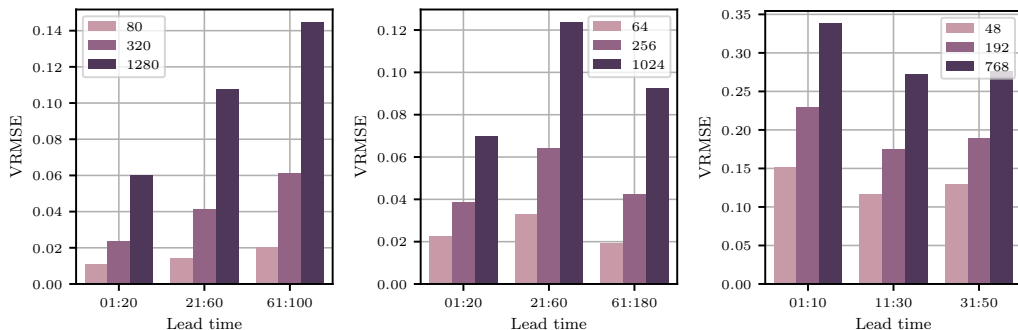


Figure 3. Average VRMSE of the autoencoder reconstruction at different compression rates and lead time horizons for the Euler (left), RB (center) and TGC (right) datasets. The compression rate has a clear impact on reconstruction quality.

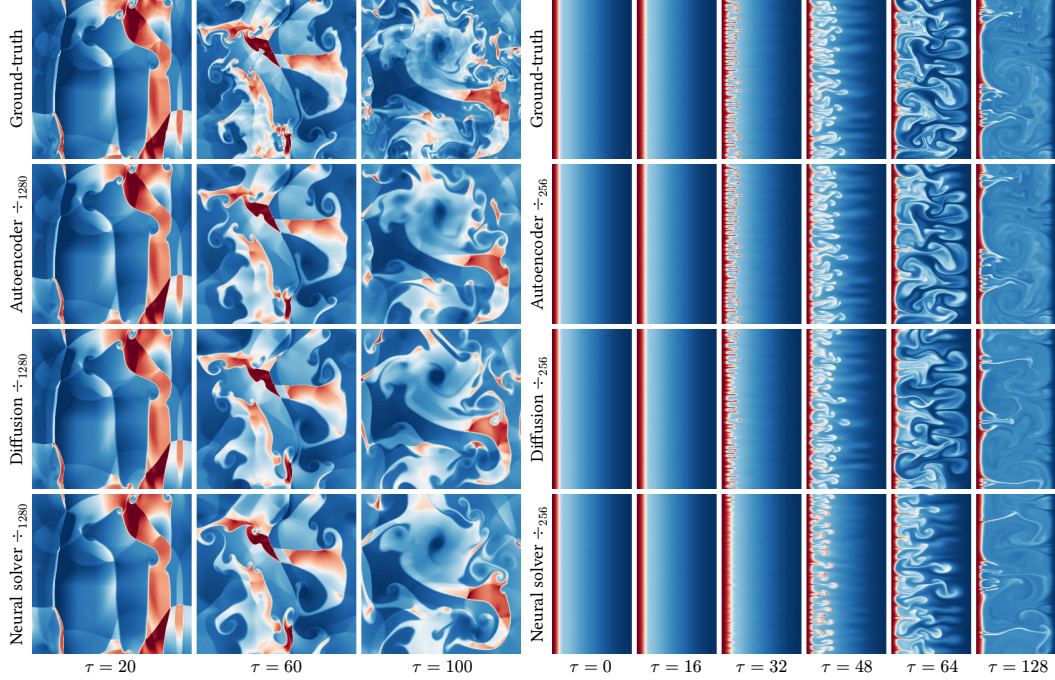


Figure 4. Examples of latent-space emulation for the Euler (left) and Rayleigh-Bénard (right) datasets. Even for large compression rates ( $\div$ ), latent-space emulators are able to reproduce the dynamics surprisingly faithfully, despite significant reconstruction artifacts. For Euler, wavefronts are accurately propagated until the end of the simulation, while vortices are well located, but distorted. For Rayleigh-Bénard, diffusion-based emulators produce plumes that grow at the correct pace but diverge from the ground-truth. Similar observations can be made in Figures 10 to 21.

As expected from imperfect emulators, the emulation error grows with the lead time, as shown in Figures 5 and 8. However, the point-wise error of diffusion models, as measured by the VRMSE, does not grow (Euler, TGC) and sometimes decreases (RB) with higher compression rates. Even at extreme ( $> 1000$ ) compression rates, latent-space emulators outperform the baseline pixel-space neural solver, despite the latter benefiting from more parameters and training compute. Similar observations can be made with the power spectrum RMSE over low and mid-frequency bands. High-frequency content, however, appears limited by the autoencoder’s reconstruction capabilities. We confirm this hypothesis by recomputing the metrics relative to the auto-encoded state  $D_\psi(E_\psi(x^i))$ , which we report in Figure 9. This time, the power spectrum RMSE of the diffusion models is low for mid and high-frequency bands. These findings support a puzzling narrative: emulation accuracy exhibits strong resilience to latent-space compression, starkly contrasting with the clear degradation in reconstruction quality.

Our experiments also provide a direct comparison between generative (diffusion) and deterministic (neural solver) approaches to emulation within a latent space. Figures 8 and 9 indicate that diffusion-based emulators are consistently more accurate than their deterministic counterparts and generate trajectories that are statistically more plausible in terms of power spectrum. This can be observed qualitatively in Figure 4 or Figures 10 to 21 in Appendix C. In addition, the spread-skill ratio of diffusion models is close to 1, suggesting that the ensemble of trajectories they produce are reasonably well calibrated in terms of uncertainty. However, the ratio slightly decreases with the compression rate. This phenomenon is partially explained by the smoothing effect of  $L_2$ -driven compression, and is therefore less severe in Figure 9. Nonetheless, it remains present and could be a sign of overfitting due to the reduced amount of training data in latent space.

Table 1. Inference time per state for the Euler dataset, including generation and decoding.

Method	Space	Time
simulator	pixel	$\mathcal{O}(10\text{ s})$
neural solver	pixel	56 ms
neural solver	latent	13 ms
diffusion	pixel	$\mathcal{O}(1\text{ s})$
diffusion	latent	84 ms

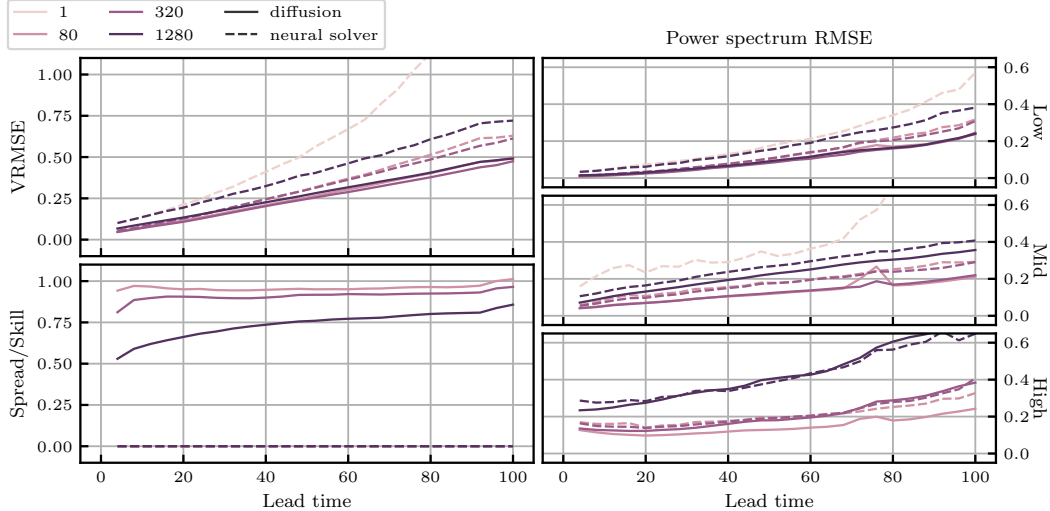


Figure 5. Average evaluation metrics of latent-space emulation for the Euler dataset. As expected from imperfect emulators, the emulation error grows with the lead time. However, the compression rate has little to no impact on diffusion-based emulation accuracy, beside high-frequency content. The spread-skill ratio [25, 75] drops slightly with the compression rate, which could be a sign of overfitting. Diffusion-based emulators are consistently more accurate than neural solvers.

In terms of computational cost, although they remain slower than latent-space neural solvers, latent-space diffusion models are much faster than their pixel-space counterparts and competitive with pixel-space neural solvers (see Table 1). With our latent diffusion models, generating and decoding a full (100 simulation steps, 7 autoregressive steps) Euler trajectory takes 3 seconds on a single A100 GPU, compared to roughly 1 CPU-hour with the original numerical simulation [38, 77].

A final advantage of diffusion models lies in their capacity to incorporate additional information during sampling via guidance methods [42, 78–81]. For example, if partial or noisy state observations are available, we can guide the emulation such that it remains consistent with these observations. We provide an illustrative example in Figure 6 where guidance is performed with the MMPS [78] method. Thanks to the additional information in the observations, the emulation diverges less from the ground-truth.

## 5 Related work

Data-driven emulation of dynamical systems has become a prominent research area [8–17] with diverse applications, including accelerating fluid simulations on uniform meshes using convolutional networks [8, 12], emulating various physics on non-uniform meshes with graph neural networks [9–11, 14], and solving partial differential equations with neural operators [13, 21, 82–84]. However, McCabe et al. [15] and Herde et al. [16] highlight the large data requirements of these methods and propose pre-training on multiple data-abundant physics before fine-tuning on data-scarce ones to improve data efficiency and generalization. Our experiments similarly suggest that large datasets are needed to train latent-space emulators.

A parallel line of work, related to reduced-order modeling [85], focuses on learning low-dimensional representations of high-dimensional system states. Within this latent space, dynamics can be emulated more efficiently [86–94]. Various embedding approaches have been explored: convolutional autoencoders for uniform meshes [88, 89], graph-based autoencoders for non-uniform meshes [90], and implicit neural representations for discretization-free states [34, 92]. Koopman operator theory [95] has also been integrated into autoencoder training to promote linear latent dynamics [91, 96]. Other approaches to enhance latent predictability include regularizing temporal derivatives [97], jointly optimizing the decoder and latent emulator [98], and self-supervised prediction [99]. While our work adopts this latent emulation paradigm, we do not impose structural biases on the latent space beside reconstruction quality.

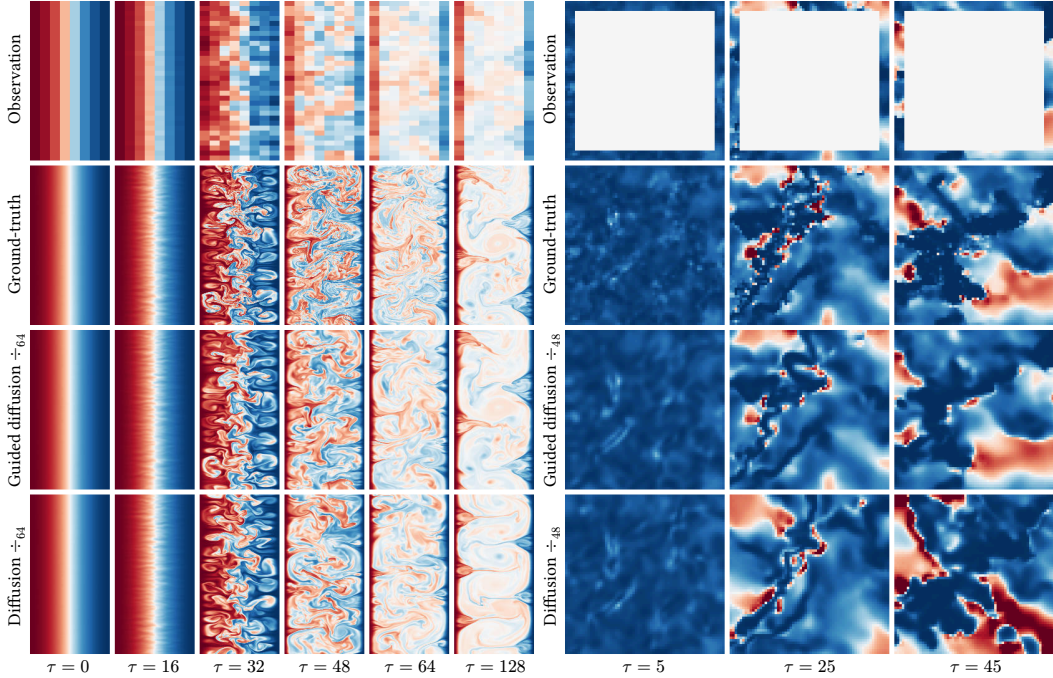


Figure 6. Example of guided latent-space emulation for the RB (left) and TGC (right) datasets. The observations are the states downsampled by a factor 16 for RB and a stripe along the domain boundaries for TGC. Guidance is performed using the MMPS [78] method. Thanks to the additional information in the observations, the emulation diverges less from the ground-truth.

A persistent challenge in neural emulation is ensuring temporal stability. Many models, while accurate for short-term prediction, exhibit long-term instabilities as errors accumulate, pushing the predictions out of the training data distribution [21]. Several strategies have been proposed to mitigate this issue: autoregressive unrolling during training [11, 86, 100], architectural modifications [21, 83], noise injection [12], and post-processing [18, 101]. Generative models, particularly diffusion models, have recently emerged as a promising approach to address this problem [18, 19, 22–25] as they produce statistically plausible states, even when they diverge from the ground-truth solution.

While more accurate and stable, diffusion models are computationally expensive at inference. Drawing inspiration from latent space generation in computer vision [26–32], recent studies have applied latent diffusion models to emulate dynamical systems: Gao et al. [33] address short-term precipitation forecasting, Zhou et al. [35] generate trajectories conditioned on text descriptions, Du et al. [34] generate trajectories within an implicit neural representation, and Li et al. [36] combine a state-wise autoencoder with a spatiotemporal diffusion transformer [27] for autoregressive emulation, similar to our approach. These studies report favorable or competitive results against pixel-space and deterministic baselines, consistent with our observations.

## 6 Discussion

Our results reveal key insights about latent physics emulation. First, diffusion-based emulation accuracy is surprisingly robust to latent-space compression, with performance remaining constant or even improving when autoencoder reconstruction quality significantly deteriorates. This observation is consistent with the latent generative modeling literature [26, 56], where compression serves a dual purpose: reducing dimensionality and filtering out perceptually irrelevant patterns that might distract from semantically meaningful information. Our experiments support this hypothesis as latent-space emulators outperform their pixel-space counterparts despite using fewer parameters and requiring less training compute. Yao et al. [102] similarly demonstrate that higher compression can sometimes improve generation quality despite degrading reconstruction. While our findings seem to violate the famous data processing inequality, they are well aligned with the theory of *usable* information [103], where a learned representation can hold more  $\mathcal{V}$ -information from the point

of view of a computationally constrained observer. Second, diffusion-based generative emulators consistently achieve higher ensemble accuracy than deterministic neural solvers while producing diverse, statistically plausible trajectories. This supports the idea that generative models mitigate distribution shift [18, 19, 22–25]. However, at the first prediction step, before distribution shift can take effect, diffusion models are already more accurate than deterministic neural solvers. This suggests an inherent modeling advantage, possibly lying in the iterative nature of diffusion sampling.

Despite the finite number of datasets, we believe that our findings are likely to generalize well across the broader spectrum of fluid dynamics. The Euler, RB and TGC datasets represent distinct fluid regimes that cover many key challenges in dynamical systems emulation: nonlinearities, multi-scale interactions, and complex spatio-temporal patterns. In addition, previous studies [33–36] come to similar conclusions for other fluid dynamics problems. However, we exercise caution about extending these conclusions beyond fluids. Systems governed by fundamentally different physics, such as chemical or quantum phenomena, may respond unpredictably to latent compression. Probing these boundaries represents an important direction for future research. Our empirical findings also prompt the need for theoretical explanations, which we leave to future work.

Apart from datasets, if compute resources were not a limiting factor, our study could be extended along several dimensions, although we anticipate that additional experiments would not fundamentally alter our conclusions. First, we could investigate techniques for improving the structure of the latent representation, such as incorporating Koopman-inspired losses [91, 96], regularizing temporal derivatives [97], or training shallow auxiliary decoders [102, 104]. Second, we could probe the behavior of different embedding strategies under high compression, including spatio-temporal embeddings [34, 35, 105], implicit neural representations [34, 92], and masked auto-encoders [104, 106]. Third, we could add the capability to trade speed for accuracy, analogous to running numerical solvers at finer resolutions, by training an auto-encoder with an adaptive latent dimensionality [107–109]. Forth, we could study the effects of autoencoder and emulator capacity by scaling either up or down their number of trainable parameters. Each of these directions represents a substantial computational investment, particularly given the scale of our datasets and models, but would help establish best practices for latent-space emulation.

Nevertheless, our findings lead to clear recommendations for practitioners wishing to implement physics emulators. First, try latent-space approaches before pixel-space emulation. The former offer reduced computational requirements, lower memory footprint, and comparable or better accuracy across a wide range of compression rates. Second, prefer diffusion-based emulators over deterministic neural solvers. Latent diffusion models provide more accurate, diverse and stable long-term trajectories, while narrowing the inference speed gap significantly.

Our experiments, however, reveal important considerations about dataset scale when training latent-space emulators. The decreasing spread-skill ratio observed at higher compression rates suggests potential overfitting. This makes intuitive sense: as compression increases, the effective size of the dataset in latent space decreases, making overfitting more likely at fixed model capacity. Benchmarking latent emulators on smaller (10-100 GB) datasets like those used by Kohl et al. [19] could therefore yield misleading results. In addition, because the latent space is designed to preserve pixel space content, observing overfitting in this compressed representation suggests that pixel-space models encounter similar issues that remain undetected. This points towards the need for large training datasets or mixtures of datasets used to pre-train emulators before fine-tuning on targeted physics, as advocated by McCabe et al. [15] and Herde et al. [16].

## Acknowledgments and Disclosure of Funding

We thank Géraud Krawezik and the Scientific Computing Core at the Flatiron Institute, a division of the Simons Foundation, for the compute facilities and support. We gratefully acknowledge use of the research computing resources of the Empire AI Consortium, Inc., with support from the State of New York, the Simons Foundation, and the Secunda Family Foundation. Polymathic AI acknowledges funding from the Simons Foundation and Schmidt Sciences, LLC. François Rozet is a research fellow of the F.R.S.-FNRS (Belgium) and acknowledges its financial support.

## References

- [1] ECMWF. “IFS documentation CY49R1 - part III: Dynamics and numerical procedures”. In *IFS Documentation CY49R1*. ECMWF, 2024.
- [2] Jongil Han and Hua-Lu Pan. “Revision of Convection and Vertical Diffusion Schemes in the NCEP Global Forecast System”. In *Weather and Forecasting* 26.4 (2011).
- [3] A. J. Hundhausen and R. A. Gentry. “Numerical simulation of flare-generated disturbances in the solar wind”. In *Journal of Geophysical Research (1896-1977)* 74.11 (1969).
- [4] John T. Mariska et al. “Numerical Simulations of Impulsively Heated Solar Flares”. In *The Astrophysical Journal* 341 (1989).
- [5] Chi Wang et al. “Magnetohydrodynamics (MHD) numerical simulations on the interaction of the solar wind with the magnetosphere: A review”. In *Science China Earth Sciences* 56.7 (2013).
- [6] Yuri N. Dnestrovskii and Dimitri P. Kostomarov. “Numerical Simulation of Plasmas”. Berlin, Heidelberg: Springer, 1986.
- [7] Yildirim Suzen et al. “Numerical Simulations of Plasma Based Flow Control Applications”. In *35th AIAA Fluid Dynamics Conference and Exhibit*. Fluid Dynamics and Co-located Conferences. American Institute of Aeronautics and Astronautics, 2005.
- [8] Jonathan Tompson et al. “Accelerating Eulerian Fluid Simulation With Convolutional Networks”. In *Proceedings of the 34th International Conference on Machine Learning*. PMLR, 2017.
- [9] Alvaro Sanchez-Gonzalez et al. “Learning to Simulate Complex Physics with Graph Networks”. In *Proceedings of the 37th International Conference on Machine Learning*. PMLR, 2020.
- [10] Tobias Pfaff et al. “Learning Mesh-Based Simulation with Graph Networks”. In *International Conference on Learning Representations*. 2021.
- [11] Johannes Brandstetter et al. “Message Passing Neural PDE Solvers”. In *International Conference on Learning Representations*. 2022.
- [12] Kim Stachenfeld et al. “Learned Simulators for Turbulence”. In *International Conference on Learning Representations*. 2022.
- [13] Nikola Kovachki et al. “Neural Operator: Learning Maps Between Function Spaces With Applications to PDEs”. In *Journal of Machine Learning Research* 24.89 (2023).
- [14] Remi Lam et al. “Learning skillful medium-range global weather forecasting”. In *Science* 382.6677 (2023).
- [15] Michael McCabe et al. “Multiple Physics Pretraining for Spatiotemporal Surrogate Models”. In *Advances in Neural Information Processing Systems*. Vol. 37. 2024.
- [16] Maximilian Herde et al. “Poseidon: Efficient Foundation Models for PDEs”. In *Advances in Neural Information Processing Systems*. Vol. 37. 2024.
- [17] Rudy Morel et al. “DISCO: learning to DISCover an evolution Operator for multi-physics-agnostic prediction”. 2025.
- [18] Phillip Lippe et al. “PDE-Refiner: Achieving Accurate Long Rollouts with Neural PDE Solvers”. In *Advances in Neural Information Processing Systems*. Vol. 36. 2023.
- [19] Georg Kohl et al. “Benchmarking Autoregressive Conditional Diffusion Models for Turbulent Flow Simulation”. In *ICML 2024 AI for Science Workshop*. 2024.
- [20] Björn List et al. “Learned turbulence modelling with differentiable fluid solvers: physics-based loss functions and optimisation horizons”. In *Journal of Fluid Mechanics* 949 (2022).
- [21] Michael McCabe et al. “Towards Stability of Autoregressive Neural Operators”. In *Transactions on Machine Learning Research* (2023).
- [22] Salva Cachay et al. “DYffusion: A Dynamics-informed Diffusion Model for Spatiotemporal Forecasting”. In *Advances in Neural Information Processing Systems*. Vol. 36. 2023.
- [23] Aliaksandra Shysheya et al. “On conditional diffusion models for PDE simulations”. In *Advances in Neural Information Processing Systems*. Vol. 37. 2024.
- [24] Jiahe Huang et al. “DiffusionPDE: Generative PDE-Solving under Partial Observation”. In *Advances in Neural Information Processing Systems*. Vol. 37. 2024.

- [25] Ilan Price et al. “Probabilistic weather forecasting with machine learning”. In *Nature* 637.8044 (2025).
- [26] Robin Rombach et al. “High-Resolution Image Synthesis With Latent Diffusion Models”. In *Conference on Computer Vision and Pattern Recognition*. 2022.
- [27] William Peebles and Saining Xie. “Scalable Diffusion Models with Transformers”. In *International Conference on Computer Vision*. 2023.
- [28] Patrick Esser et al. “Scaling Rectified Flow Transformers for High-Resolution Image Synthesis”. 2024.
- [29] Tero Karras et al. “Analyzing and Improving the Training Dynamics of Diffusion Models”. In *Proceedings of the IEEE/CVF Conference on Computer Vision and Pattern Recognition*. 2024.
- [30] Enze Xie et al. “SANA: Efficient High-Resolution Text-to-Image Synthesis with Linear Diffusion Transformers”. In *International Conference on Learning Representations*. 2025.
- [31] Junyu Chen et al. “Deep Compression Autoencoder for Efficient High-Resolution Diffusion Models”. In *International Conference on Learning Representations*. 2025.
- [32] Adam Polyak et al. “Movie Gen: A Cast of Media Foundation Models”. 2024.
- [33] Zhihan Gao et al. “PreDiff: Precipitation Nowcasting with Latent Diffusion Models”. In *Thirty-seventh Conference on Neural Information Processing Systems*. 2023.
- [34] Pan Du et al. “Conditional neural field latent diffusion model for generating spatiotemporal turbulence”. In *Nature Communications* 15.1 (2024).
- [35] Anthony Zhou et al. “Text2PDE: Latent Diffusion Models for Accessible Physics Simulation”. In *International Conference on Learning Representations*. 2025.
- [36] Zijie Li et al. “Generative Latent Neural PDE Solver using Flow Matching”. 2025.
- [37] Gérôme Andry et al. “Appa: Bending Weather Dynamics with Latent Diffusion Models for Global Data Assimilation”. 2025.
- [38] Ruben Ohana et al. “The Well: a Large-Scale Collection of Diverse Physics Simulations for Machine Learning”. In *Advances in Neural Information Processing Systems*. Vol. 37. 2024.
- [39] Jascha Sohl-Dickstein et al. “Deep Unsupervised Learning using Nonequilibrium Thermodynamics”. In *Proceedings of the 32nd International Conference on Machine Learning*. 2015.
- [40] Jonathan Ho et al. “Denoising Diffusion Probabilistic Models”. In *Advances in Neural Information Processing Systems*. 2020.
- [41] Yang Song and Stefano Ermon. “Generative Modeling by Estimating Gradients of the Data Distribution”. In *Advances in Neural Information Processing Systems*. 2019.
- [42] Yang Song et al. “Score-Based Generative Modeling through Stochastic Differential Equations”. In *International Conference on Learning Representations*. 2021.
- [43] Brian D. O. Anderson. “Reverse-time diffusion equation models”. In *Stochastic Processes and their Applications* 12.3 (1982).
- [44] Simo Särkkä and Arno Solin. “Applied Stochastic Differential Equations”. Institute of Mathematical Statistics Textbooks. Cambridge University Press, 2019.
- [45] Shanchuan Lin et al. “Common Diffusion Noise Schedules and Sample Steps are Flawed”. In *2024 IEEE/CVF Winter Conference on Applications of Computer Vision (WACV)*. 2024.
- [46] Xingchao Liu et al. “Flow Straight and Fast: Learning to Generate and Transfer Data with Rectified Flow”. In *International Conference on Learning Representations*. 2023.
- [47] Yaron Lipman et al. “Flow Matching for Generative Modeling”. In 2023.
- [48] Aapo Hyvärinen. “Estimation of Non-Normalized Statistical Models by Score Matching”. In *Journal of Machine Learning Research* (2005).
- [49] Pascal Vincent. “A Connection Between Score Matching and Denoising Autoencoders”. In *Neural Computation* (2011).
- [50] Jiaming Song et al. “Denoising Diffusion Implicit Models”. In *International Conference on Learning Representations*. 2021.
- [51] Tero Karras et al. “Elucidating the Design Space of Diffusion-Based Generative Models”. In *Advances in Neural Information Processing Systems*. 2022.

- [52] M. C. K. Tweedie. “Functions of a statistical variate with given means, with special reference to Laplacian distributions”. In *Mathematical Proceedings of the Cambridge Philosophical Society* (1947).
- [53] Bradley Efron. “Tweedie’s Formula and Selection Bias”. In *Journal of the American Statistical Association* (2011).
- [54] Kwanyoung Kim and Jong Chul Ye. “Noise2Score: Tweedie’s Approach to Self-Supervised Image Denoising without Clean Images”. In *Advances in Neural Information Processing Systems*. 2021.
- [55] Chenlin Meng et al. “Estimating High Order Gradients of the Data Distribution by Denoising”. In *Advances in Neural Information Processing Systems*. 2021.
- [56] Sander Dieleman. “Generative modelling in latent space”. 2025.
- [57] Richard Zhang et al. “The Unreasonable Effectiveness of Deep Features as a Perceptual Metric”. In *Conference on Computer Vision and Pattern Recognition*. 2018.
- [58] Ian J. Goodfellow et al. “Generative Adversarial Networks”. 2014.
- [59] Patrick Esser et al. “Taming Transformers for High-Resolution Image Synthesis”. In *Proceedings of the IEEE/CVF Conference on Computer Vision and Pattern Recognition*. 2021.
- [60] Xi-Lin Li. “Preconditioned Stochastic Gradient Descent”. In *IEEE Transactions on Neural Networks and Learning Systems* 29.5 (2018).
- [61] Vineet Gupta et al. “Shampoo: Preconditioned Stochastic Tensor Optimization”. In *Proceedings of the 35th International Conference on Machine Learning*. PMLR, 2018.
- [62] Nikhil Vyas et al. “SOAP: Improving and Stabilizing Shampoo using Adam for Language Modeling”. In *International Conference on Learning Representations*. 2025.
- [63] Diederik P. Kingma and Jimmy Ba. “Adam: A Method for Stochastic Optimization”. In *International Conference on Learning Representations*. 2015.
- [64] Lucas Nestler and François Fleuret. “HeavyBall: Efficient optimizers”. 2022.
- [65] Vikram Voleti et al. “MCVD - Masked Conditional Video Diffusion for Prediction, Generation, and Interpolation”. In *Advances in Neural Information Processing Systems*. Vol. 35. 2022.
- [66] Alex Henry et al. “Query-Key Normalization for Transformers”. In *Findings of the Association for Computational Linguistics*. Ed. by Trevor Cohn et al. Online: Association for Computational Linguistics, 2020.
- [67] Jianlin Su et al. “RoFormer: Enhanced transformer with Rotary Position Embedding”. In *Neurocomputing* 568 (2024).
- [68] Byeongho Heo et al. “Rotary Position Embedding for Vision Transformer”. In *European Conference on Computer Vision*. Ed. by Aleš Leonardis et al. Cham: Springer Nature Switzerland, 2025.
- [69] Zhanchao Zhou et al. “Value Residual Learning”. 2024.
- [70] Zilong Huang et al. “CCNet: Criss-Cross Attention for Semantic Segmentation”. In *Proceedings of the IEEE/CVF International Conference on Computer Vision*. 2019.
- [71] Jonathan Ho et al. “Axial Attention in Multidimensional Transformers”. 2019.
- [72] Ali Hassani et al. “Neighborhood Attention Transformer”. In *Proceedings of the IEEE/CVF Conference on Computer Vision and Pattern Recognition*. 2023.
- [73] Qinsheng Zhang and Yongxin Chen. “Fast Sampling of Diffusion Models with Exponential Integrator”. In *International Conference on Learning Representations*. 2023.
- [74] Alexey Dosovitskiy et al. “An Image is Worth 16x16 Words: Transformers for Image Recognition at Scale”. In *International Conference on Learning Representations*. 2021.
- [75] V. Fortin et al. “Why Should Ensemble Spread Match the RMSE of the Ensemble Mean?” In *Journal of Hydrometeorology* 15.4 (2014).
- [76] Hugh L. Dryden. “A Review of the Statistical Theory of Turbulence”. In *Quarterly of Applied Mathematics* 1.1 (1943).
- [77] Kyle T. Mandli et al. “Clawpack: building an open source ecosystem for solving hyperbolic PDEs”. In *PeerJ Computer Science* 2 (2016).
- [78] François Fleuret et al. “Learning Diffusion Priors from Observations by Expectation Maximization”. In *Advances in Neural Information Processing Systems*. Vol. 37. 2024.

- [79] Jonathan Ho et al. “Video Diffusion Models”. In *ICLR Workshop on Deep Generative Models for Highly Structured Data*. 2022.
- [80] Hyungjin Chung et al. “Diffusion Posterior Sampling for General Noisy Inverse Problems”. In *International Conference on Learning Representations*. 2023.
- [81] François Rozet and Gilles Louppe. “Score-based Data Assimilation”. In *Advances in Neural Information Processing Systems*. Vol. 36. 2023.
- [82] Zongyi Li et al. “Fourier Neural Operator for Parametric Partial Differential Equations”. In *International Conference on Learning Representations*. 2021.
- [83] Bogdan Raonic et al. “Convolutional Neural Operators for robust and accurate learning of PDEs”. In *Advances in Neural Information Processing Systems*. Vol. 36. 2023.
- [84] Zhongkai Hao et al. “GNOT: A General Neural Operator Transformer for Operator Learning”. In *Proceedings of the 40th International Conference on Machine Learning*. PMLR, 2023.
- [85] Peter Benner et al. “A Survey of Projection-Based Model Reduction Methods for Parametric Dynamical Systems”. In *SIAM Review* 57.4 (2015).
- [86] Bethany Lusch et al. “Deep learning for universal linear embeddings of nonlinear dynamics”. In *Nature Communications* 9.1 (2018).
- [87] Hugo F. S. Lui and William R. Wolf. “Construction of reduced-order models for fluid flows using deep feedforward neural networks”. In *Journal of Fluid Mechanics* 872 (2019).
- [88] S. Wiewel et al. “Latent Space Physics: Towards Learning the Temporal Evolution of Fluid Flow”. In *Computer Graphics Forum* 38.2 (2019).
- [89] Romit Maulik et al. “Reduced-order modeling of advection-dominated systems with recurrent neural networks and convolutional autoencoders”. In *Physics of Fluids* 33.3 (2021).
- [90] Xu Han et al. “Predicting Physics in Mesh-reduced Space with Temporal Attention”. In *International Conference on Learning Representations*. 2022.
- [91] Nicholas Geneva and Nicholas Zabaras. “Transformers for modeling physical systems”. In *Neural Networks* 146 (2022).
- [92] Peter Yichen Chen et al. “CROM: Continuous Reduced-Order Modeling of PDEs Using Implicit Neural Representations”. In *International Conference on Learning Representations*. 2023.
- [93] AmirPouya Hemmasian and Amir Barati Farimani. “Reduced-order modeling of fluid flows with transformers”. In *Physics of Fluids* 35.5 (2023).
- [94] Zijie Li et al. “Latent neural PDE solver: A reduced-order modeling framework for partial differential equations”. In *Journal of Computational Physics* 524 (2025).
- [95] B. O. Koopman. “Hamiltonian Systems and Transformation in Hilbert Space”. In *Proceedings of the National Academy of Sciences* 17.5 (1931).
- [96] Enoch Yeung et al. “Learning Deep Neural Network Representations for Koopman Operators of Nonlinear Dynamical Systems”. In *American Control Conference (ACC)*. 2019.
- [97] Xiaoyu Xie et al. “Smooth and Sparse Latent Dynamics in Operator Learning with Jerk Regularization”. 2024.
- [98] Francesco Regazzoni et al. “Learning the intrinsic dynamics of spatio-temporal processes through Latent Dynamics Networks”. In *Nature Communications* 15.1 (2024).
- [99] Adrien Bardes et al. “Revisiting Feature Prediction for Learning Visual Representations from Video”. In *Transactions on Machine Learning Research* (2024).
- [100] Nicholas Geneva and Nicholas Zabaras. “Modeling the dynamics of PDE systems with physics-constrained deep auto-regressive networks”. In *Journal of Computational Physics* 403 (2020).
- [101] Daniel E. Worrall et al. “Spectral Shaping for Neural PDE Surrogates”. 2024.
- [102] Jingfeng Yao et al. “Reconstruction vs. Generation: Taming Optimization Dilemma in Latent Diffusion Models”. 2025.
- [103] Yilun Xu et al. “A Theory of Usable Information under Computational Constraints”. In *International Conference on Learning Representations*. 2019.
- [104] Hao Chen et al. “Masked Autoencoders Are Effective Tokenizers for Diffusion Models”. 2025.

- [105] Lijun Yu et al. “MAGVIT: Masked Generative Video Transformer”. In *Proceedings of the IEEE/CVF Conference on Computer Vision and Pattern Recognition*. 2023.
- [106] Kaiming He et al. “Masked Autoencoders Are Scalable Vision Learners”. In *2022 IEEE/CVF Conference on Computer Vision and Pattern Recognition (CVPR)*. 2022.
- [107] Alekh Karkada Ashok and Nagaraju Palani. “Autoencoders with Variable Sized Latent Vector for Image Compression”. In *Proceedings of the IEEE Conference on Computer Vision and Pattern Recognition Workshops*. 2018.
- [108] Chi-Hieu Pham et al. “PCA-AE: Principal Component Analysis Autoencoder for Organising the Latent Space of Generative Networks”. In *Journal of Mathematical Imaging and Vision* 64.5 (2022).
- [109] Roman Bachmann et al. “FlexTok: Resampling Images into 1D Token Sequences of Flexible Length”. In *Forty-second International Conference on Machine Learning*. 2025.
- [110] Keaton J. Burns et al. “Dedalus: A flexible framework for numerical simulations with spectral methods”. In *Physical Review Research* 2.2 (2020).
- [111] Keiya Hirashima et al. “3D-Spatiotemporal forecasting the expansion of supernova shells using deep learning towards high-resolution galaxy simulations”. In *Monthly Notices of the Royal Astronomical Society* 526.3 (2023).
- [112] Kaiming He et al. “Deep Residual Learning for Image Recognition”. In *Conference on Computer Vision and Pattern Recognition*. 2016.
- [113] Stefan Elfwing et al. “Sigmoid-weighted linear units for neural network function approximation in reinforcement learning”. In *Neural Networks*. Special issue on deep reinforcement learning 107 (2018).
- [114] Jimmy Lei Ba et al. “Layer Normalization”. 2016.
- [115] Nicolas Bonneel et al. “Sliced and Radon Wasserstein Barycenters of Measures”. In *Journal of Mathematical Imaging and Vision* (2015).
- [116] Soheil Kolouri et al. “Generalized Sliced Wasserstein Distances”. In *Advances in Neural Information Processing Systems*. Vol. 32. Curran Associates, Inc., 2019.
- [117] Tung Nguyen et al. “PhysiX: A Foundation Model for Physics Simulations”. 2025.
- [118] Zhikai Wu et al. “TANTE: Time-Adaptive Operator Learning via Neural Taylor Expansion”. 2025.
- [119] Payel Mukhopadhyay et al. “Controllable Patching for Compute-Adaptive Surrogate Modeling of Partial Differential Equations”. 2025.
- [120] Laurens van der Maaten and Geoffrey Hinton. “Visualizing Data using t-SNE”. In *Journal of Machine Learning Research* 9.86 (2008).
- [121] Gabriel Peyré and Marco Cuturi. “Computational Optimal Transport: With Applications to Data Science”. In *Foundations and Trends in Machine Learning* 11.5-6 (2019).

## A Spread / Skill

The skill [25, 75] of an ensemble of  $K$  particles  $v_k$  is defined as the RMSE of the ensemble mean

$$\text{Skill} = \sqrt{\left\langle \left( u - \frac{1}{K} \sum_{k=1}^K v_k \right)^2 \right\rangle} \quad (11)$$

where  $\langle \cdot \rangle$  denotes the spatial mean operator. The spread is defined as the ensemble standard deviation

$$\text{Spread} = \sqrt{\left\langle \left( \frac{1}{K-1} \sum_{j=1}^K \left( v_j - \frac{1}{K} \sum_{k=1}^K v_k \right)^2 \right) \right\rangle}. \quad (12)$$

Under these definitions and the assumption of a perfect forecast where ensemble particles are exchangeable, Fortin et al. [75] show that

$$\text{Skill} \approx \sqrt{\frac{K+1}{K}} \text{ Spread}. \quad (13)$$

This motivates the use of the (corrected) spread-skill ratio as a metric. Intuitively, if the ratio is smaller than one, the ensemble is biased or under-dispersed. If the ratio is larger than one, the ensemble is over-dispersed. It should be noted however, that a spread-skill ratio of 1 is a necessary but not sufficient condition for a perfect forecast.

## B Experiment details

**Datasets** For all datasets, each field is standardized with respect to its mean and variance over the training set. For Euler, the non-negative scalar fields (energy, density, pressure) are transformed with  $x \mapsto \log(x + 1)$  before standardization. For TGC, the non-negative scalar fields (density, pressure, temperature) are transformed with  $x \mapsto \log(x + 10^{-6})$  before standardization. When the states are illustrated graphically, as in Figure 1, we represent the density field for Euler, the buoyancy field for RB, and a slice of the temperature field for TGC.

Table 2. Details of the selected datasets. We refer the reader to Ohana et al. [38] for more information.

	Euler Multi-Quadrants	Rayleigh-Bénard	Turbulence Gravity Cooling
Software	Clawpack [77]	Dedalus [110]	ASURA-FDPS [111]
Size	5243 GB	367 GB	849 GB
Fields	energy, density, pressure, velocity	buoyancy, pressure, momentum	density, pressure, temperature, velocity
Channels $C_{\text{pixel}}$	5	4	6
Resolution	$512 \times 512$	$512 \times 128$	$64 \times 64 \times 64$
Discretization	Uniform	Chebyshev	Uniform
Trajectories	10000	1750	2700
Time steps $L$	100	200	50
Stride $\Delta$	4	1	1
$\theta$	heat capacity $\gamma$ , boundary conditions	Rayleigh number, Prandtl number	hydrogen density $\rho_0$ , temperature $T_0$ , metallicity $Z$

**Autoencoders** The encoder  $E_\psi$  and decoder  $D_\psi$  are convolutional networks with residual blocks [112], SiLU [113] activation functions and layer normalization [114]. The output of the encoder is transformed with a saturating function (see Section 3). We provide a schematic illustration of the autoencoder architecture in Figure 7. Following McCabe et al. [15], we use a field-weighted loss  $\ell$ , and choose the variance-normalized MSE (VMSE)

$$\text{VMSE}(u, v) = \frac{\langle (u - v)^2 \rangle}{\langle (u - \langle u \rangle)^2 \rangle + \epsilon} \quad (14)$$

averaged over fields, where  $\epsilon = 10^{-2}$  mitigates training instabilities. We train the encoder and decoder jointly for  $1024 \times 256$  steps of the PSGD [60] optimizer. To mitigate overfitting we use random spatial axes permutations, flips and rolls as data augmentation. Each autoencoder takes 1 (RB), 2 (Euler) or 4 (TGC) days to train on 8 H100 GPUs. Other hyperparameters are provided in Table 3.

**Caching** The entire dataset is encoded with each trained autoencoder and the resulting latent trajectories are cached permanently on disk. The latter can then be used to train latent-space emulators, without needing to load and encode high-dimensional samples on the fly. Depending on hardware and data dimensionality, this approach can make a huge difference in I/O efficiency.

**Emulators** The denoiser  $d_\phi$  and neural solver  $f_\phi$  are transformers with query-key normalization [66], rotary positional embedding (RoPE) [67, 68], and value residual learning [69]. The 16 blocks are modulated by the simulation parameters  $\theta$  and the diffusion time  $t$ , as in diffusion transformers [27]. We train the emulator for  $4096 \times 64$  steps of the Adam [63] optimizer. Each latent-space emulator takes 2 (RB) or 5 (Euler, TGC) days to train on 8 H100 GPUs. Each pixel-space emulator takes 5 (RB) or 10 (Euler) days to train on 16 H100 GPUs. We do not train a pixel-space emulator for TGC. Other hyperparameters are provided in Table 5.

During training we randomly sample the binary mask  $b$ . The number of context elements  $c$  follows a Poisson distribution  $\text{Pois}(\lambda = 2)$  truncated between 1 and  $n$ . Hence, the masks  $b$  take the form

$$b = (\underbrace{1, \dots, 1}_c, 0, \dots, 0) \quad (15)$$

implicitly defining a distribution  $p(b)$ .

Table 3. Hyperparameters for the autoencoders.

	Euler & RB	TGC
Architecture	Conv	Conv
Parameters	$3.1 \times 10^8$	$7.2 \times 10^8$
Pixel shape	$C_{\text{pixel}} \times H \times W$	$C_{\text{pixel}} \times H \times W \times Z$
Latent shape	$C_{\text{latent}} \times \frac{H}{32} \times \frac{W}{32}$	$C_{\text{latent}} \times \frac{H}{8} \times \frac{W}{8} \times \frac{Z}{8}$
Residual blocks per level	(3, 3, 3, 3, 3, 3)	(3, 3, 3, 3)
Channels per level	(64, 128, 256, 512, 768, 1024)	(64, 256, 512, 1024)
Kernel size	$3 \times 3$	$3 \times 3 \times 3$
Activation	SiLU	SiLU
Normalization	LayerNorm	LayerNorm
Dropout	0.05	0.05
Loss	VMSE	VMSE
Optimizer	PSGD	PSGD
Learning rate	$10^{-5}$	$10^{-5}$
Weight decay	0.0	0.0
Scheduler	cosine	cosine
Gradient norm clipping	1.0	1.0
Batch size	64	64
Steps per epoch	256	256
Epochs	1024	1024
GPUs	8	8

Table 4. Short ablation study on the autoencoder architecture and training configurations. We pick the Rayleigh-Bénard dataset and an architecture with 64 latent channels to perform this study. The two major modifications that we propose are (1) the initialization of the downsampling and upsampling layers near identity, inspired by Chen et al. [31], and (2) the use of a preconditioned optimizer, PSGD [60], instead of Adam [63]. We report the mean absolute error (MAE) on the validation set during training. The combination of both proposed modifications leads to order(s) of magnitude faster convergence.

Optimizer	Id. init	Epoch			Time
		10	100	1000	
Adam	w/o	0.065	0.029	0.017	19 h
Adam	w/	0.039	0.023	0.014	19 h
PSGD	w/	0.023	0.015	0.011	25 h

**Evaluation** For each dataset, we randomly select 64 trajectories  $x^{0:L}$  with various parameters  $\theta$  in the test set. For each latent-space emulator, we encode the initial state  $z_0 = E_\psi(x_0)$  and produce 16 distinct autoregressive rollouts  $z^{1:L}$ . For the diffusion models, sampling is performed with 16 steps of the 3rd order Adams-Bashforth multi-step integration method [73]. The metrics (VRMSE, power spectrum RMSE, spread-skill ratio) are then measured between the predicted states  $\hat{x}^i = D_\psi(z^i)$  and the ground-truth states  $x^i$  or the auto-encoded states  $D_\psi(E_\psi(x^i))$ .

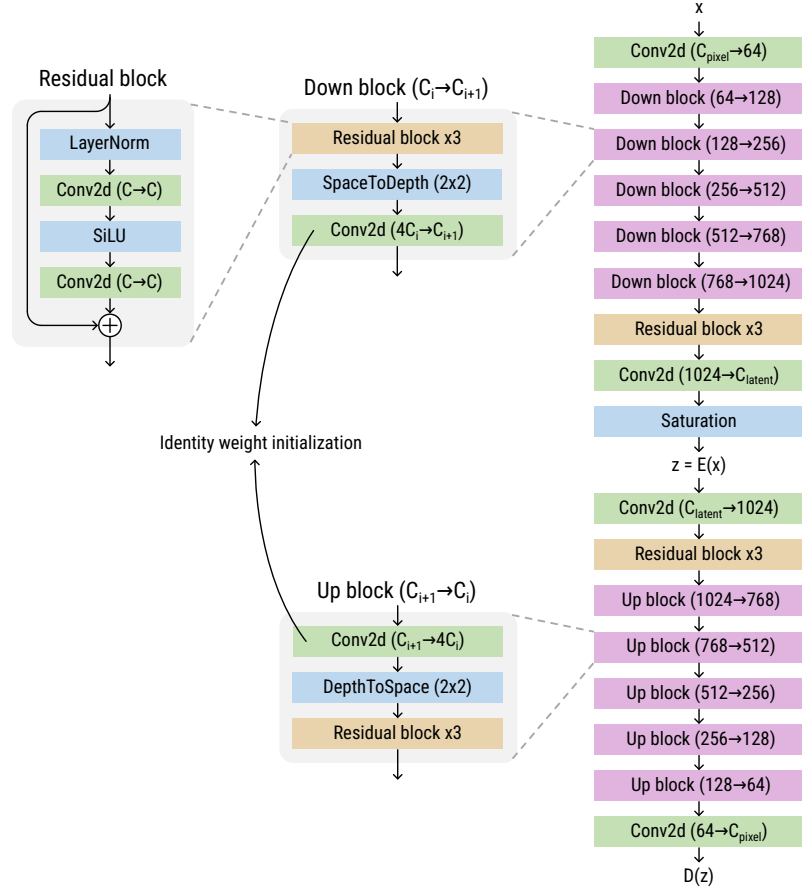


Figure 7. Schematic representation of the autoencoder architecture. Downsampling (resp. upsampling) is performed with a space-to-depth (resp. depth-to-space) operation followed (resp. preceded) with a convolution initialized near identity.

Table 5. Hyperparameters for the emulators.

	Latent-space	Pixel-space
Architecture	Transformer	Transformer
Parameters	$2.2 \times 10^8$	$8.6 \times 10^8$
Input shape	$C_{\text{latent}} \times (n+1) \times \frac{H}{32} \times \frac{W}{32}$	$C_{\text{pixel}} \times (n+1) \times H \times W$
Patch size	$1 \times 1 \times 1$	$1 \times 16 \times 16$
Tokens	$(n+1) \times \frac{H}{32} \times \frac{W}{32}$	$(n+1) \times \frac{H}{16} \times \frac{W}{16}$
Embedding size	1024	2048
Blocks	16	16
Positional embedding	Absolute + RoPE	Absolute + RoPE
Activation	SiLU	SiLU
Normalization	LayerNorm	LayerNorm
Dropout	0.05	0.05
Optimizer	Adam	Adam
Learning rate	$10^{-4}$	$10^{-4}$
Weight decay	0.0	0.0
Scheduler	cosine	cosine
Gradient norm clipping	1.0	1.0
Batch size	256	256
Steps per epoch	64	64
Epochs	4096	4096
GPUs	8	16

### C Additional emulation results

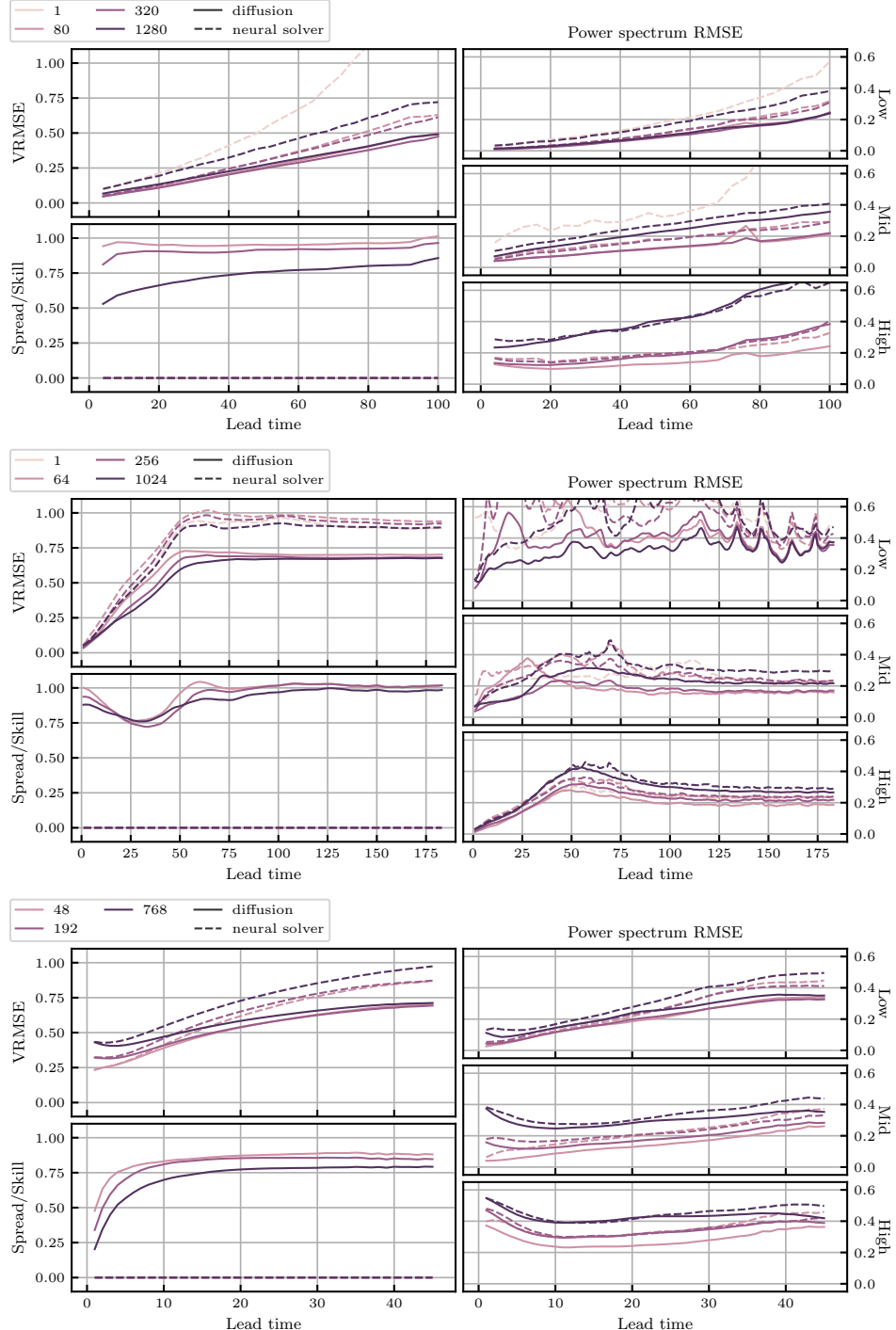


Figure 8. Average evaluation metrics of latent-space emulation for the Euler (top), RB (center) and TGC (bottom) datasets. As expected from imperfect emulators, the emulation error grows with the lead time. However, increasing the compression rate does not degrade (Euler, TGC) and sometimes improves (RB) the accuracy of diffusion models. The spread-skill ratio [25, 75] drops slightly with the compression rate, which could be a sign of overfitting. Diffusion-based emulators are consistently more accurate than neural solvers.

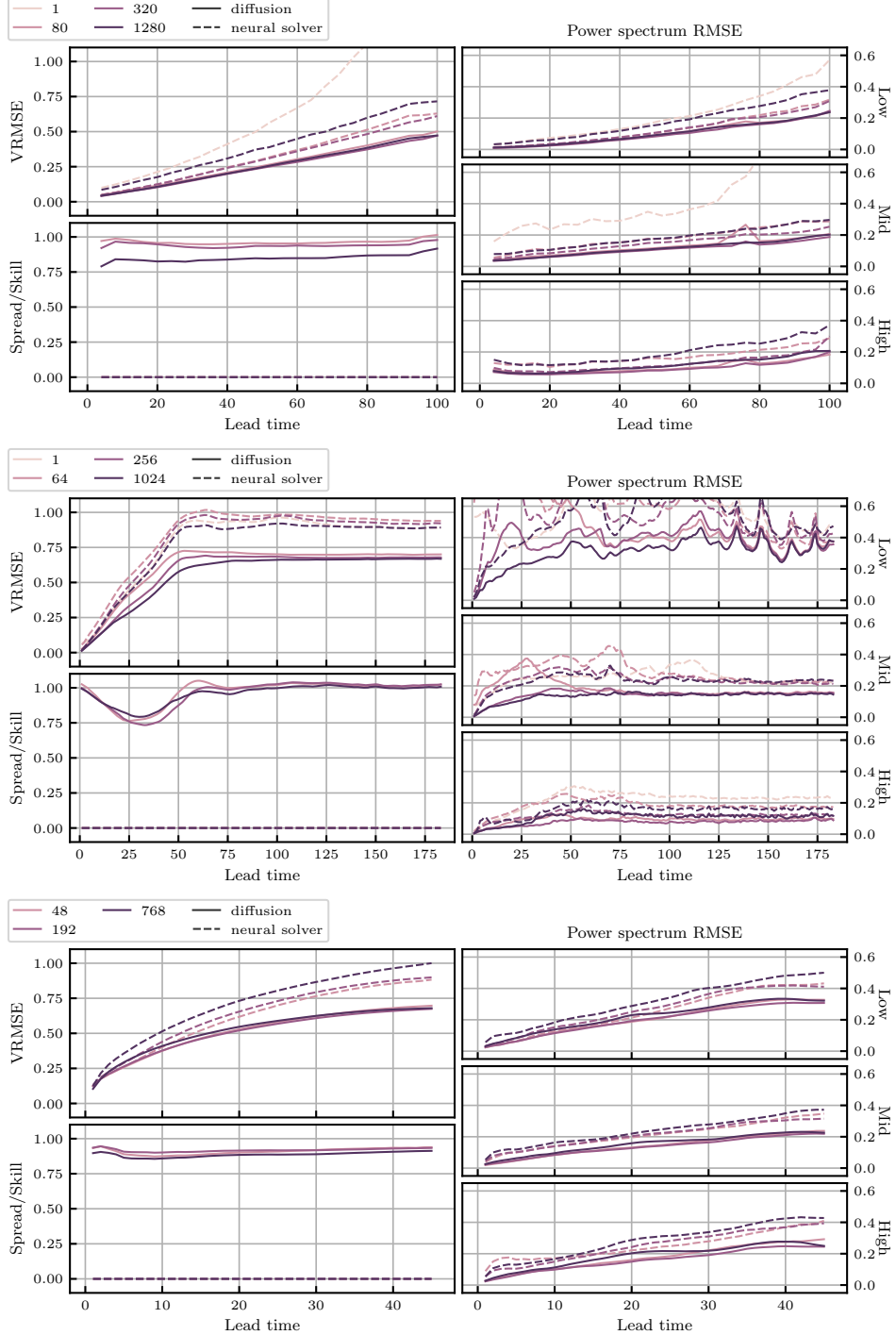


Figure 9. Average evaluation metrics of latent-space emulation relative to the auto-encoded states  $D_\psi(E_\psi(x^i))$  for the Euler (top), RB (center) and TGC (bottom) datasets. As expected from imperfect emulators, the emulation error grows with the lead time. However, increasing the compression rate does not degrade (Euler, TGC) and sometimes improves (RB) the accuracy of diffusion models. The spread-skill ratio [25, 75] drops slightly with the compression rate, which could be a sign of overfitting. Diffusion-based emulators are consistently more accurate than neural solvers.

Table 6. Average VRMSE of autoencoder reconstruction and latent-space emulation at different compression rates ( $\div$ ) and lead time horizons for the Euler, RB and TGC datasets. Increasing the compression rate has a clear impact on reconstruction quality, but does not degrade significantly (Euler, TGC) and sometimes improves (RB) the accuracy of diffusion models.

Method	Euler				Method	RB			
	$\div$	1:20	21:60	61:100		$\div$	1:20	21:60	61:180
autoencoder	80	0.011	0.014	0.020	autoencoder	64	0.023	0.033	0.019
	320	0.023	0.041	0.061		256	0.039	0.064	0.042
	1280	0.060	0.107	0.144		1024	0.070	0.124	0.092
diffusion	80	0.075	0.199	0.395	diffusion	64	0.171	0.582	0.704
	320	0.070	0.192	0.371		256	0.141	0.509	0.683
	1280	0.093	0.217	0.400		1024	0.146	0.457	0.670
neural solver	1	0.138	0.397	1.102	neural solver	1	0.185	0.681	0.918
	80	0.077	0.232	0.500		64	0.244	0.761	0.968
	320	0.080	0.232	0.476		256	0.197	0.716	0.945
	1280	0.137	0.314	0.592		1024	0.195	0.665	0.903
TGC									
Method	$\div$	1:10	11:20	21:50	Method	$\div$	1:10	11:20	21:50
	48	0.151	0.116	0.129		48	0.296	0.522	0.673
autoencoder	192	0.229	0.175	0.189	autoencoder	192	0.342	0.527	0.665
	768	0.338	0.272	0.276		768	0.425	0.575	0.694
	48	0.302	0.599	0.826		48	0.361	0.632	0.835
diffusion	192	0.361	0.632	0.835		192	0.462	0.710	0.920
	768	0.462	0.710	0.920		768	0.462	0.710	0.920
	48	0.361	0.632	0.835		48	0.462	0.710	0.920

Table 7. Average VRMSE of latent-space emulation at different context lengths ( $c$ ) and lead time horizons for the Euler, RB and TGC datasets. We can test different context lengths without retraining as our models were trained for different conditioning tasks (see Section 3). Perhaps surprisingly, context lengths does not have a significant impact on emulation accuracy.

Method	Euler			Method	RB				
	$c$	1:20	21:60	61:100	$c$	1:20	21:60	61:180	
diffusion	1	0.085	0.204	0.393	diffusion	1	0.152	0.510	0.683
	2	0.074	0.200	0.383		2	0.150	0.511	0.685
	3	0.078	0.203	0.389		3	0.157	0.527	0.689
neural solver	1	0.108	0.266	0.526	neural solver	1	0.208	0.705	0.932
	2	0.092	0.253	0.513		2	0.209	0.708	0.943
	3	0.094	0.260	0.529		3	0.220	0.728	0.940
TGC									
Method	$c$	1:10	11:20	21:50	Method	$c$	1:10	11:20	21:50
	1	0.362	0.550	0.681		1	0.351	0.535	0.669
diffusion	2	0.350	0.539	0.683		2	0.350	0.539	0.683
	3	0.350	0.539	0.683		3	0.376	0.632	0.837
	1	0.371	0.641	0.855		2	0.378	0.669	0.888
neural solver	2	0.371	0.641	0.855		3	0.378	0.669	0.888
	1	0.376	0.632	0.837		2	0.378	0.669	0.888
	3	0.378	0.669	0.888		1	0.376	0.632	0.837

Table 8. Average power spectrum RMSE of autoencoder reconstruction and latent-space emulation at different compression rates ( $\div$ ) and lead time horizons for the Euler dataset. The high-frequency content of diffusion-based emulators is limited by the autoencoder’s reconstruction capabilities.

Method	$\div$	Low			Mid			High		
		1:20	21:60	61:100	1:20	21:60	61:100	1:20	21:60	61:100
autoencoder	80	0.001	0.001	0.001	0.006	0.008	0.014	0.072	0.069	0.096
	320	0.002	0.003	0.004	0.022	0.047	0.085	0.112	0.141	0.240
	1280	0.009	0.017	0.025	0.074	0.167	0.264	0.240	0.355	0.577
diffusion	80	0.017	0.063	0.168	0.054	0.100	0.178	0.112	0.116	0.184
	320	0.014	0.058	0.157	0.052	0.102	0.171	0.128	0.155	0.275
	1280	0.019	0.065	0.163	0.096	0.187	0.300	0.246	0.349	0.569
neural solver	1	0.046	0.128	0.339	0.227	0.297	0.754	0.821	0.984	2.666
	80	0.021	0.074	0.212	0.085	0.151	0.245	0.164	0.173	0.249
	320	0.020	0.075	0.204	0.074	0.144	0.234	0.151	0.169	0.271
	1280	0.045	0.116	0.274	0.131	0.227	0.349	0.283	0.345	0.545

Table 9. Average power spectrum RMSE of autoencoder reconstruction and latent-space emulation at different compression rates ( $\div$ ) and lead time horizons for the Rayleigh-Benard dataset. The high-frequency content of diffusion-based emulators is limited by the autoencoder’s reconstruction capabilities.

Method	$\div$	Low			Mid			High		
		1:20	21:60	61:180	1:20	21:60	61:180	1:20	21:60	61:180
autoencoder	64	0.043	0.004	0.001	0.011	0.013	0.012	0.026	0.159	0.148
	256	0.061	0.011	0.004	0.028	0.080	0.075	0.050	0.220	0.212
	1024	0.121	0.033	0.018	0.063	0.186	0.197	0.076	0.294	0.294
diffusion	64	1.751	0.850	0.386	0.197	0.266	0.159	0.054	0.220	0.199
	256	0.328	0.399	0.396	0.084	0.195	0.177	0.065	0.239	0.232
	1024	0.193	0.292	0.344	0.095	0.243	0.240	0.083	0.314	0.297
neural solver	1	0.467	0.520	0.650	0.151	0.255	0.264	0.076	0.232	0.242
	64	3.625	0.915	0.566	0.268	0.351	0.275	0.099	0.279	0.257
	256	0.575	0.675	0.526	0.165	0.317	0.264	0.091	0.275	0.257
	1024	0.285	0.496	0.560	0.152	0.338	0.321	0.090	0.320	0.326

Table 10. Average power spectrum RMSE of autoencoder reconstruction and latent-space emulation at different compression rates ( $\div$ ) and lead time horizons for the TGC dataset. The high-frequency content of diffusion-based emulators is limited by the autoencoder’s reconstruction capabilities.

Method	$\div$	Low			Mid			High		
		1:10	11:30	31:50	1:10	11:30	31:50	1:10	11:30	31:50
autoencoder	48	0.011	0.016	0.025	0.023	0.026	0.044	0.275	0.188	0.195
	192	0.028	0.033	0.045	0.108	0.091	0.114	0.359	0.273	0.282
	768	0.072	0.068	0.080	0.285	0.235	0.254	0.454	0.476	0.367
diffusion	48	0.064	0.185	0.319	0.058	0.128	0.220	0.296	0.247	0.331
	192	0.069	0.191	0.311	0.128	0.164	0.252	0.369	0.316	0.384
	768	0.107	0.294	0.425	0.289	0.305	0.360	0.456	0.419	0.444
neural solver	48	0.070	0.221	0.424	0.110	0.197	0.324	0.357	0.320	0.427
	192	0.086	0.228	0.402	0.172	0.201	0.295	0.391	0.317	0.395
	768	0.138	0.277	0.465	0.322	0.305	0.407	0.471	0.418	0.493

Table 11. Average sliced earth mover’s distance (SEMD) [115, 116] of the density field of autoencoder reconstruction and latent-space emulation at different compression rates ( $\div$ ) and lead time horizons for the Euler dataset. The SEMD is small and is not significantly impacted by the compression rate, especially for diffusion models. For reference, the density fields of two consecutive states  $x^i$  and  $x^{i+1}$  have a typical SEMD of 0.0025. *Why this metric?* The Euler equations are sometimes used in aerodynamics to model flow around objects and one is typically interested in the global fluid displacement. The rationale for using this metric is that a small drift in the density field would not significantly affect the (S)EMD, while it could affect point-wise metrics heavily.

Method	EMD (density field)			
	$\div$	1:20	21:60	61:100
autoencoder	80	0.0000	0.0000	0.0000
	320	0.0001	0.0001	0.0001
	1280	0.0002	0.0003	0.0005
diffusion	80	0.0004	0.0010	0.0023
	320	0.0003	0.0009	0.0022
	1280	0.0004	0.0010	0.0023
neural solver	1	0.0011	0.0031	0.0066
	80	0.0005	0.0012	0.0028
	320	0.0004	0.0012	0.0027
	1280	0.0008	0.0020	0.0041

Table 12. Average Wasserstein distance of the distribution of vertical velocity values of autoencoder reconstruction and latent-space emulation at different compression rates ( $\div$ ) and lead time horizons for the RB dataset. The Wasserstein distance is smaller for diffusion models and decreases with the compression rate. For reference, the distributions of vertical velocity values of two consecutive states  $x^i$  and  $x^{i+1}$  have a typical Wasserstein distance of 0.004. *Why this metric?* One interesting quantity in buoyancy-driven convection is the growth speed of plumes in the fluid. The distribution of the (vertical) velocity values is a good summary statistic for tracking the growth of plumes.

Method	Wasserstein (vertical velocity field)			
	$\div$	1:20	21:60	61:180
autoencoder	64	0.0000	0.0002	0.0002
	256	0.0001	0.0007	0.0005
	1024	0.0002	0.0020	0.0018
diffusion	64	0.0003	0.0104	0.0141
	256	0.0003	0.0092	0.0141
	1024	0.0004	0.0063	0.0139
neural solver	1	0.0003	0.0153	0.0247
	64	0.0009	0.0272	0.0223
	256	0.0007	0.0197	0.0187
	1024	0.0007	0.0157	0.0206

Table 13. Average Wasserstein distance of the distribution of density values of autoencoder reconstruction and latent-space emulation at different compression rates ( $\div$ ) and lead time horizons for the TGC dataset. The Wasserstein distance is smaller for diffusion models, but grows significantly with the lead time, even for the autoencoder reconstruction. For reference, the distributions of density values of two consecutive states  $x^i$  and  $x^{i+1}$  have a typical Wasserstein distance of 0.01. *Why this metric?* In the interstellar medium, gravity forms clusters of matter that eventually lead to the birth of stars. The kind of clusters (compact, diffuse, or anything in between) and their proportions is of interest for domain-scientists. The distribution of the density values is a good summary statistic for clustering dynamics.

Method	Wasserstein (density field)			
	$\div$	1:10	11:30	31:50
autoencoder	48	0.0034	0.0048	0.0089
	192	0.0082	0.0110	0.0183
	768	0.0181	0.0236	0.0338
diffusion	48	0.0044	0.0138	0.0266
	192	0.0089	0.0172	0.0310
	768	0.0186	0.0274	0.0425
neural solver	48	0.0074	0.0253	0.0524
	192	0.0091	0.0171	0.0329
	768	0.0220	0.0296	0.0492

Table 14. Average VRMSE results from various studies using TheWell [38] datasets. Even though our latent neural solvers (LNSs) and latent diffusion models (LDMs) outperform most published baselines, we emphasize that we do not position our models as state-of-the-art, due to the discrepancies in parameters count, training and evaluation. Notably, the U-Net and FNO baselines trained by Ohana et al. [38] are much smaller than other models, and their hyper-parameters were not tuned.

Source	Method	Dataset	Parameters	Lead time	VRMSE
Ohana et al. [38]	FNO	Euler	$2 \times 10^7$	6:12	1.13
Ohana et al. [38]	U-Net	Euler	$2 \times 10^7$	6:12	1.02
Ours	ViT	Euler	$8.6 \times 10^8$	1:20	0.138
Ours	LNS $\div_{80}$	Euler	$3.1 \times 10^8 + 2.2 \times 10^8$	1:20	0.077
Ours	LDM $\div_{80}$	Euler	$3.1 \times 10^8 + 2.2 \times 10^8$	1:20	0.075
Ohana et al. [38]	FNO	RB	$2 \times 10^7$	6:12	10+
Ohana et al. [38]	U-Net	RB	$2 \times 10^7$	6:12	10+
Nguyen et al. [117]	PhysiX	RB	$4.5 \times 10^9$	2:8	1.067
Wu et al. [118]	TANTE	RB	$10^8$	1:16	0.609
Mukhopadhyay et al. [119]	ViT + CSM	RB	$10^8$	10	0.140
Ours	ViT	RB	$8.6 \times 10^8$	1:20	0.185
Ours	LNS $\div_{256}$	RB	$3.1 \times 10^8 + 2.2 \times 10^8$	1:20	0.197
Ours	LDM $\div_{256}$	RB	$3.1 \times 10^8 + 2.2 \times 10^8$	1:20	0.141
Ohana et al. [38]	FNO	TGC	$2 \times 10^7$	6:12	3.55
Ohana et al. [38]	U-Net	TGC	$2 \times 10^7$	6:12	7.14
Mukhopadhyay et al. [119]	ViT + CKM	TGC	$10^8$	10	0.527
Ours	LNS $\div_{48}$	TGC	$7.2 \times 10^8 + 2.2 \times 10^8$	1:10	0.302
Ours	LDM $\div_{48}$	TGC	$7.2 \times 10^8 + 2.2 \times 10^8$	1:10	0.296

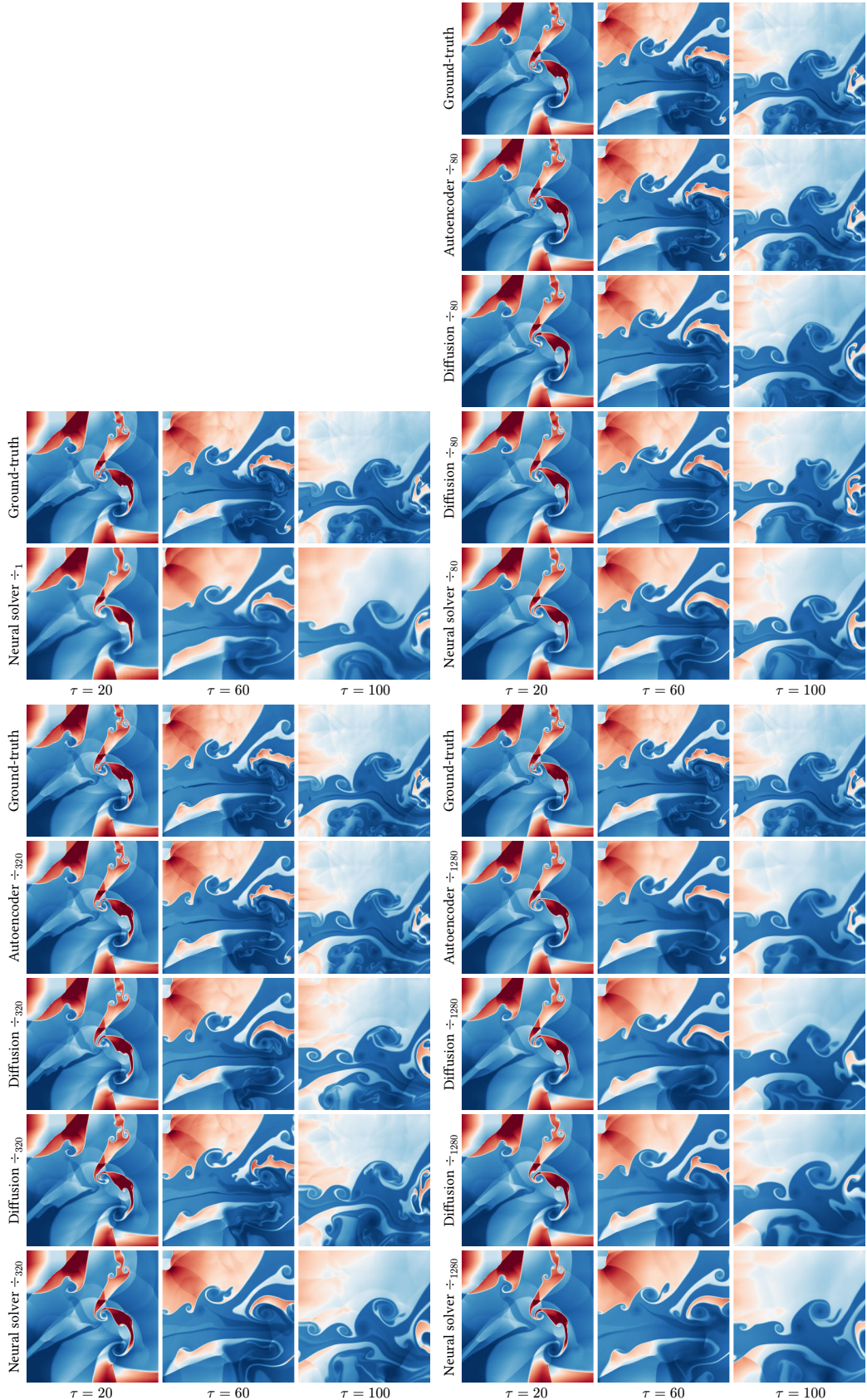


Figure 10. Examples of emulation at different compression rates ( $\div$ ) for the Euler dataset. In this simulation, the system has open boundary conditions.

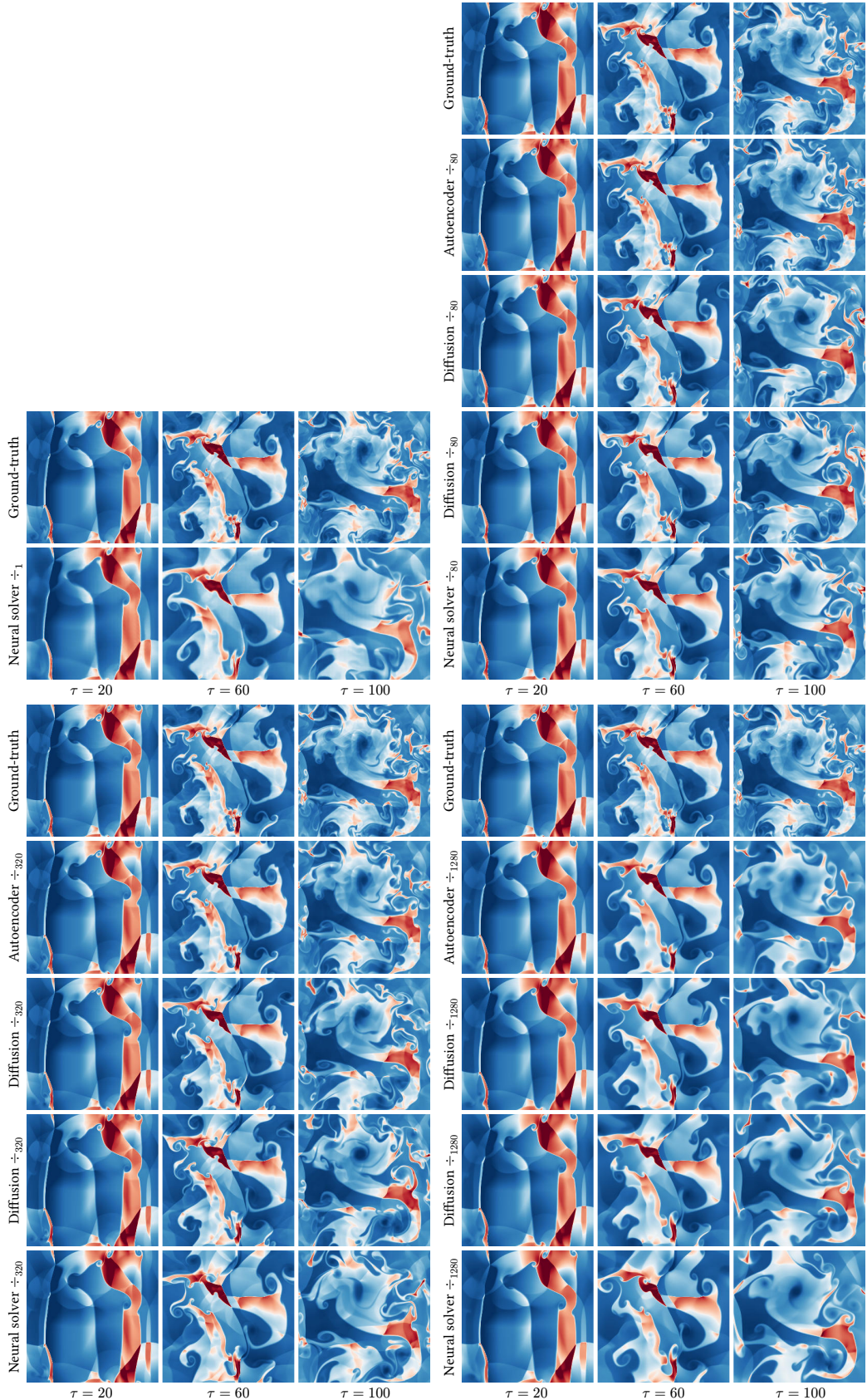


Figure 11. Examples of emulation at different compression rates ( $\div$ ) for the Euler dataset. In this simulation, the system has periodic boundary conditions.

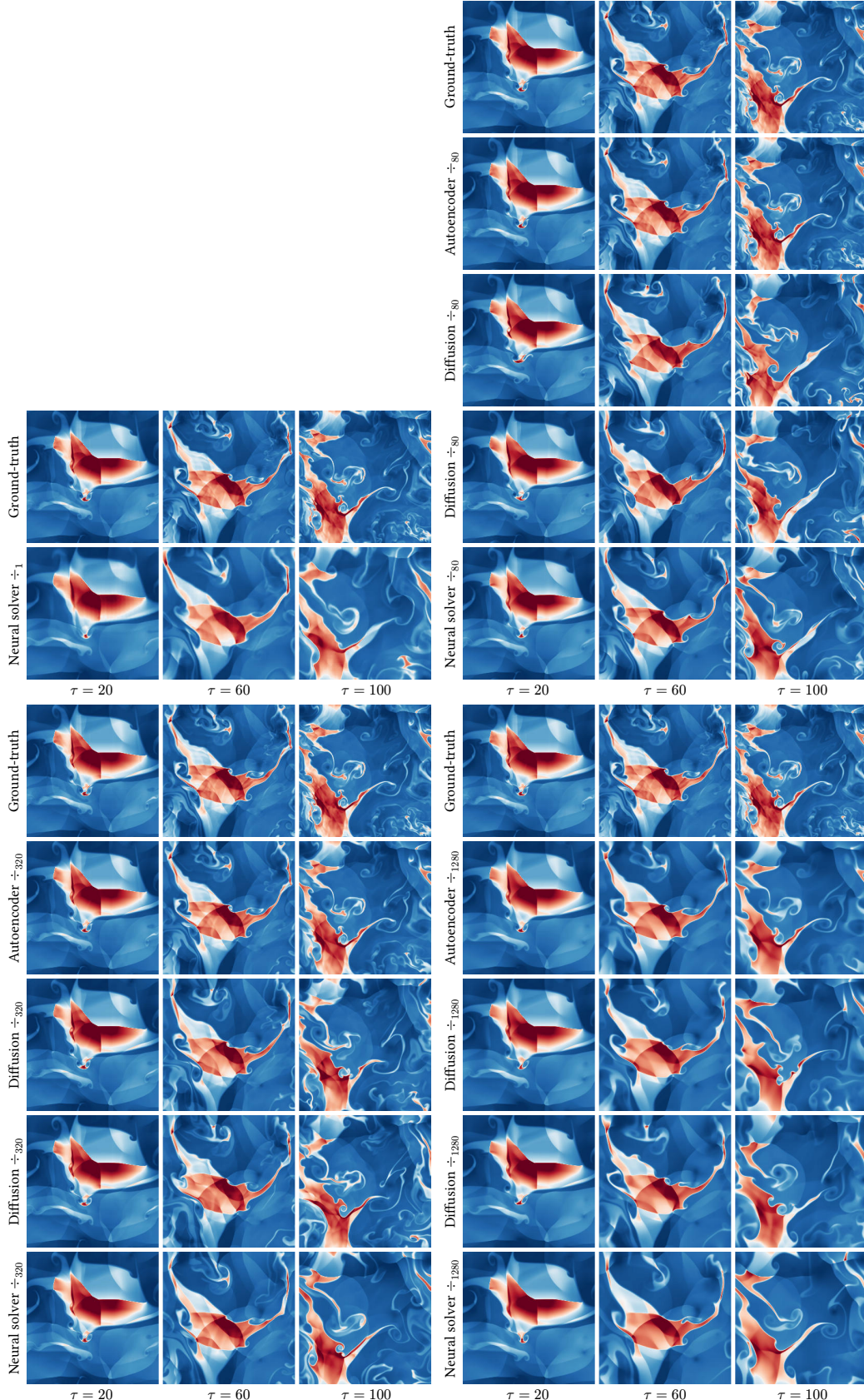


Figure 12. Examples of emulation at different compression rates ( $\div$ ) for the Euler dataset. In this simulation, the system has periodic boundary conditions.

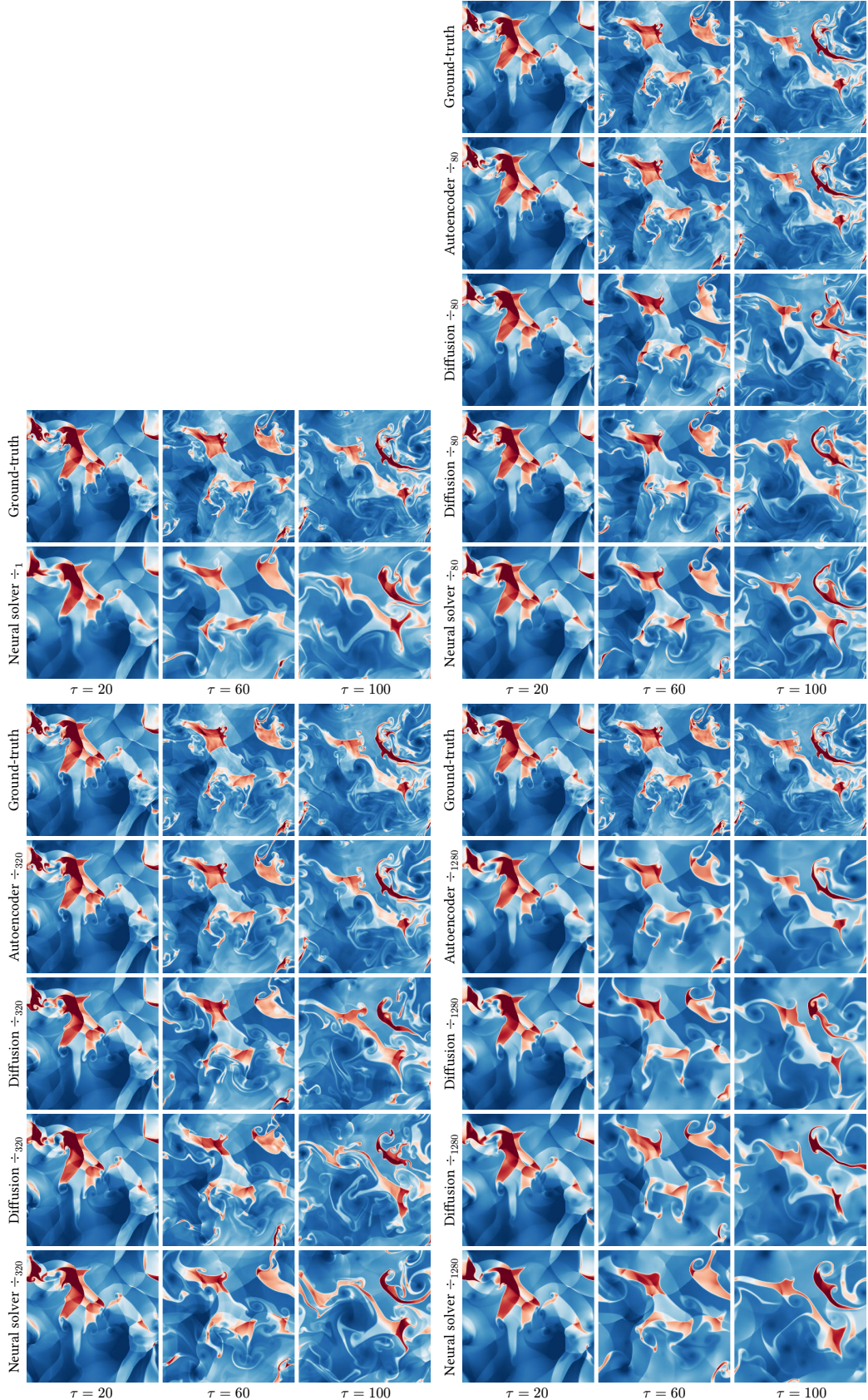


Figure 13. Examples of emulation at different compression rates ( $\div$ ) for the Euler dataset. In this simulation, the system has periodic boundary conditions.

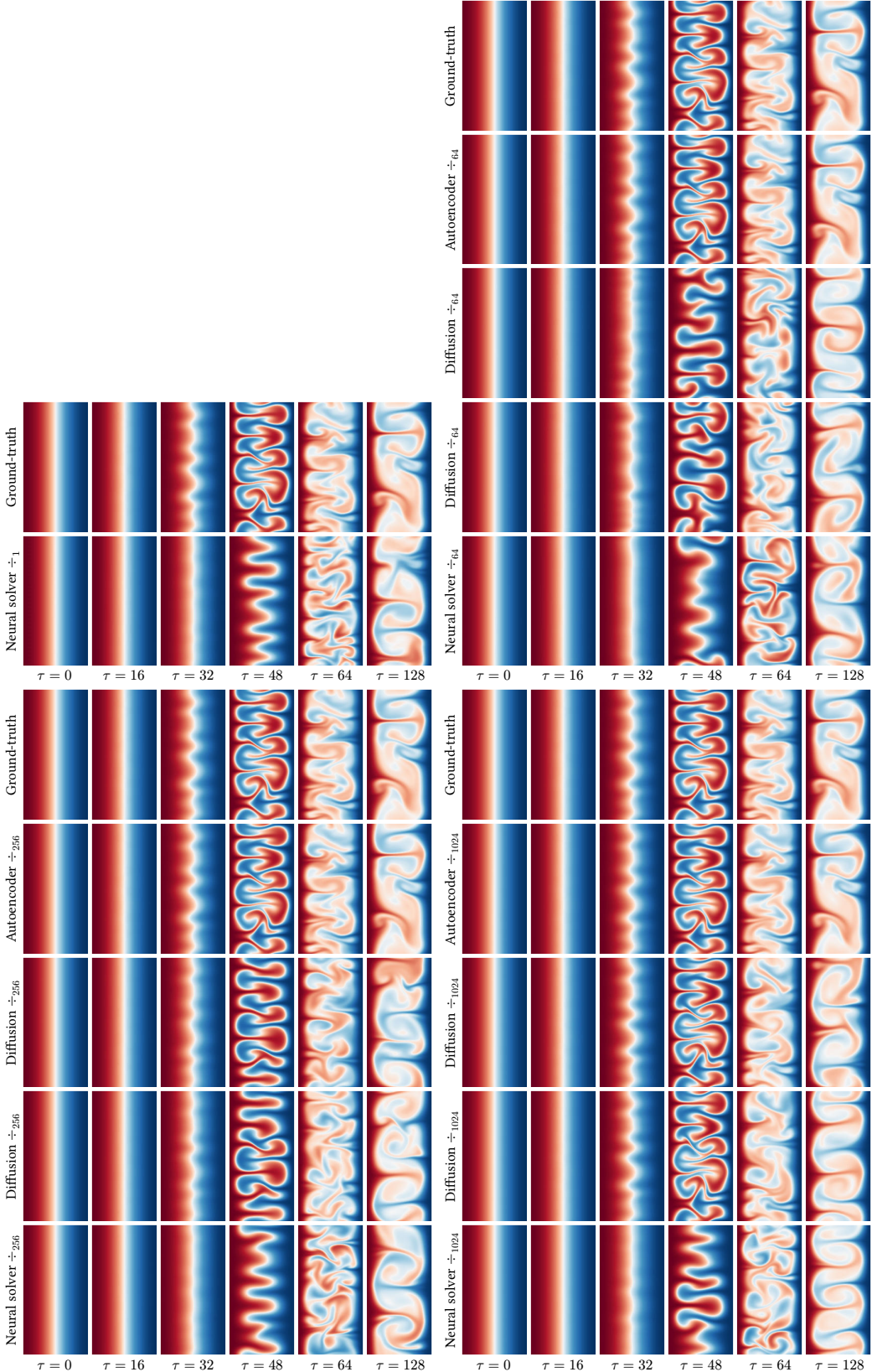


Figure 14. Examples of emulation at different compression rates ( $\div$ ) for the Rayleigh-Bénard dataset. In this simulation, the fluid is in a low-turbulence regime ( $\text{Ra} = 10^6$ ).

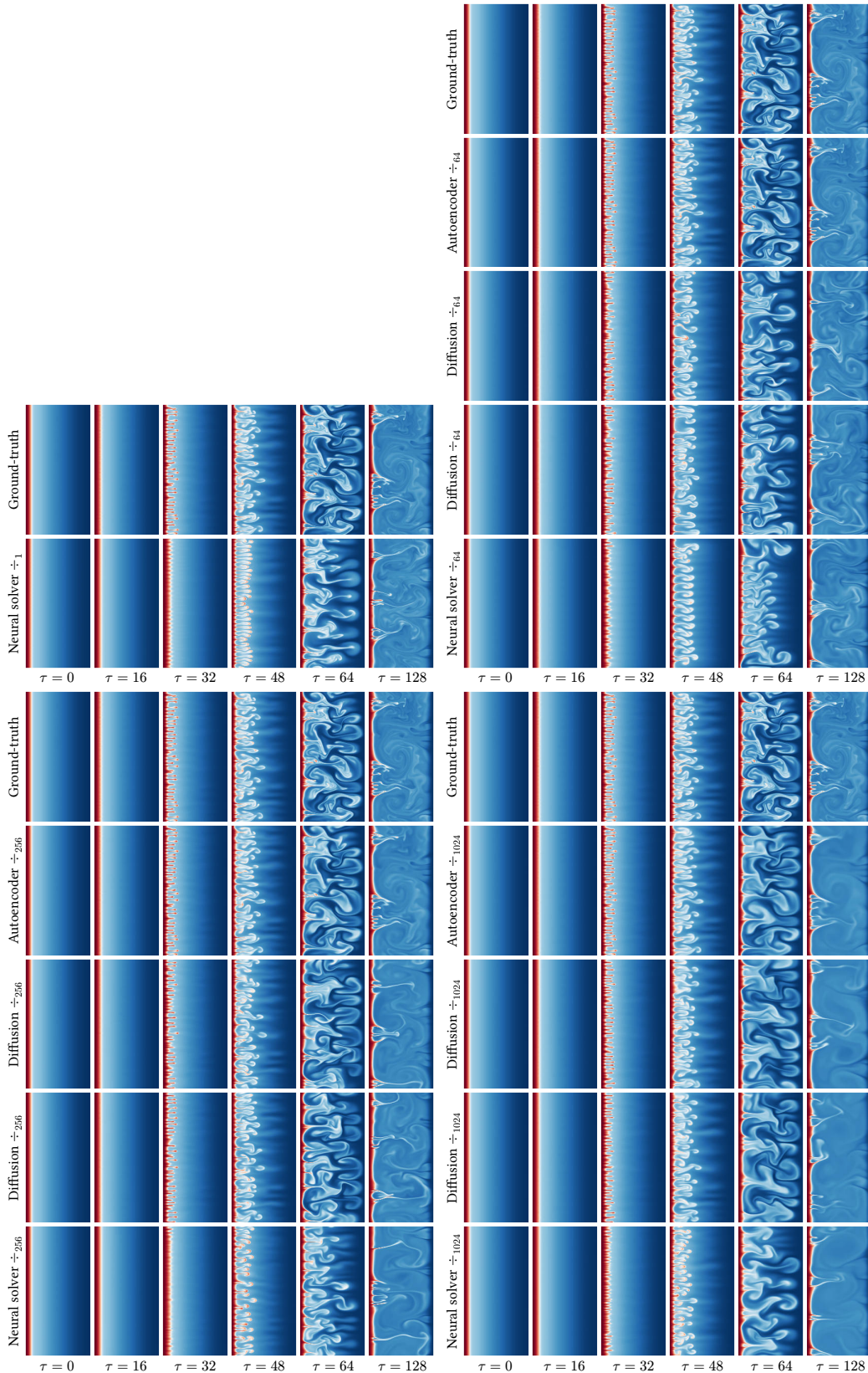


Figure 15. Examples of emulation at different compression rates ( $\div$ ) for the Rayleigh-Bénard dataset. In this simulation, the fluid is in a high-turbulence regime ( $\text{Ra} = 10^8$ ).

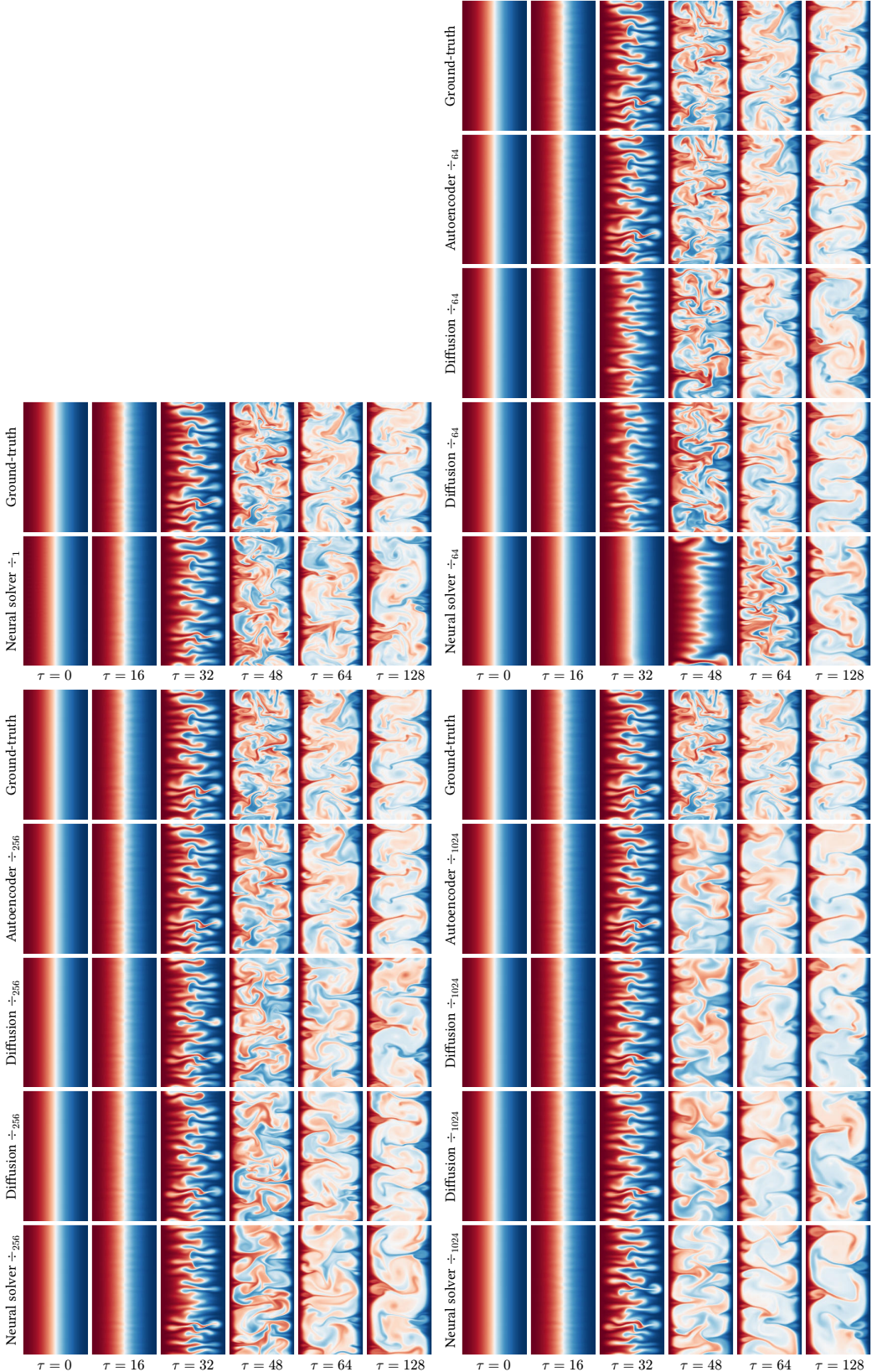


Figure 16. Examples of emulation at different compression rates ( $\div$ ) for the Rayleigh-Bénard dataset. In this simulation, the fluid is in a low-turbulence regime ( $\text{Ra} = 10^6$ ).

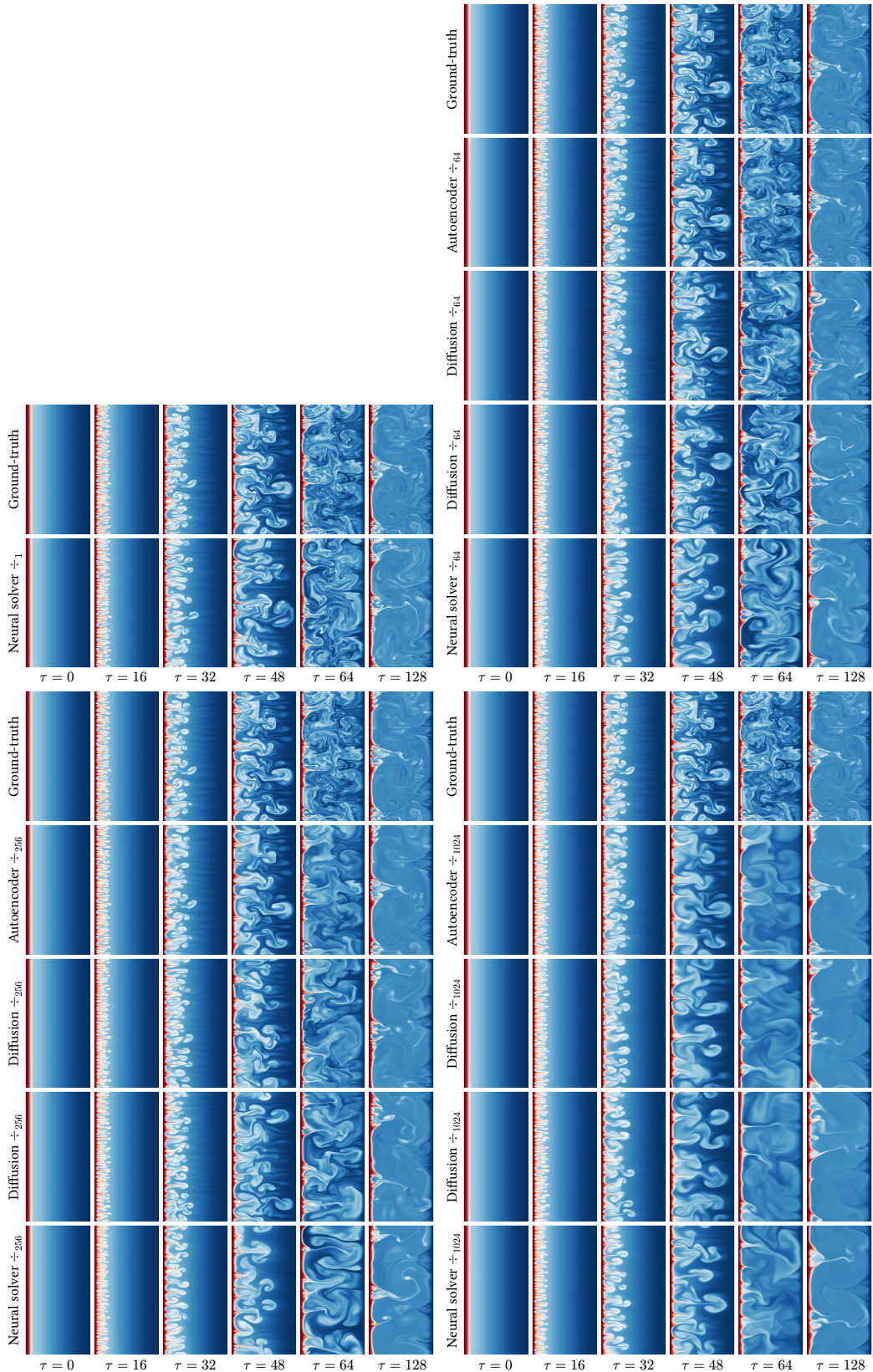


Figure 17. Examples of emulation at different compression rates ( $\div$ ) for the Rayleigh-Bénard dataset. In this simulation, the fluid is in a high-turbulence regime ( $\text{Ra} = 10^8$ ).

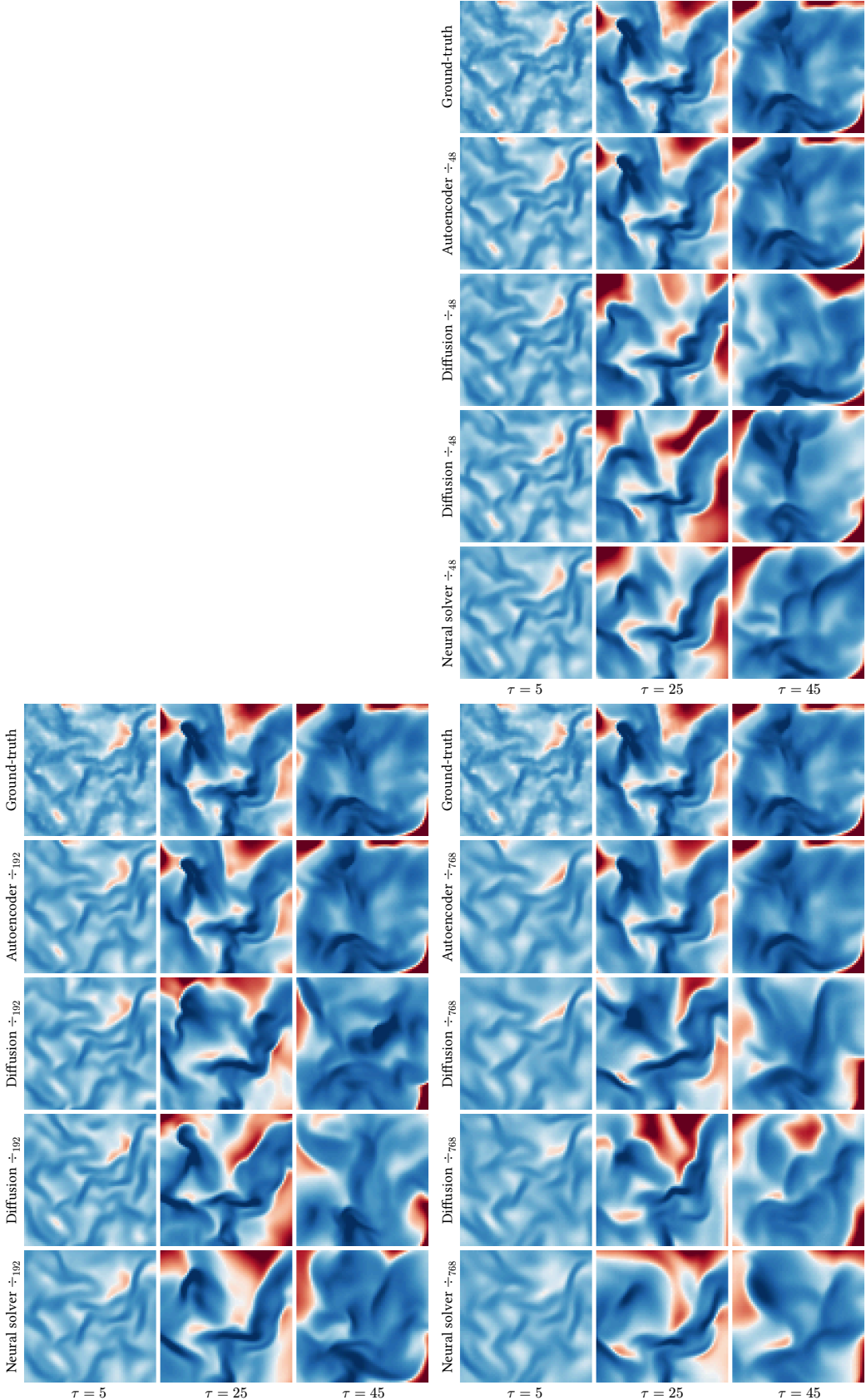


Figure 18. Examples of emulation at different compression rates ( $\div$ ) for the TGC dataset. In this simulation, the initial density is low and the initial temperature is low ( $\rho_0 = 0.445, T_0 = 10.0$ ).

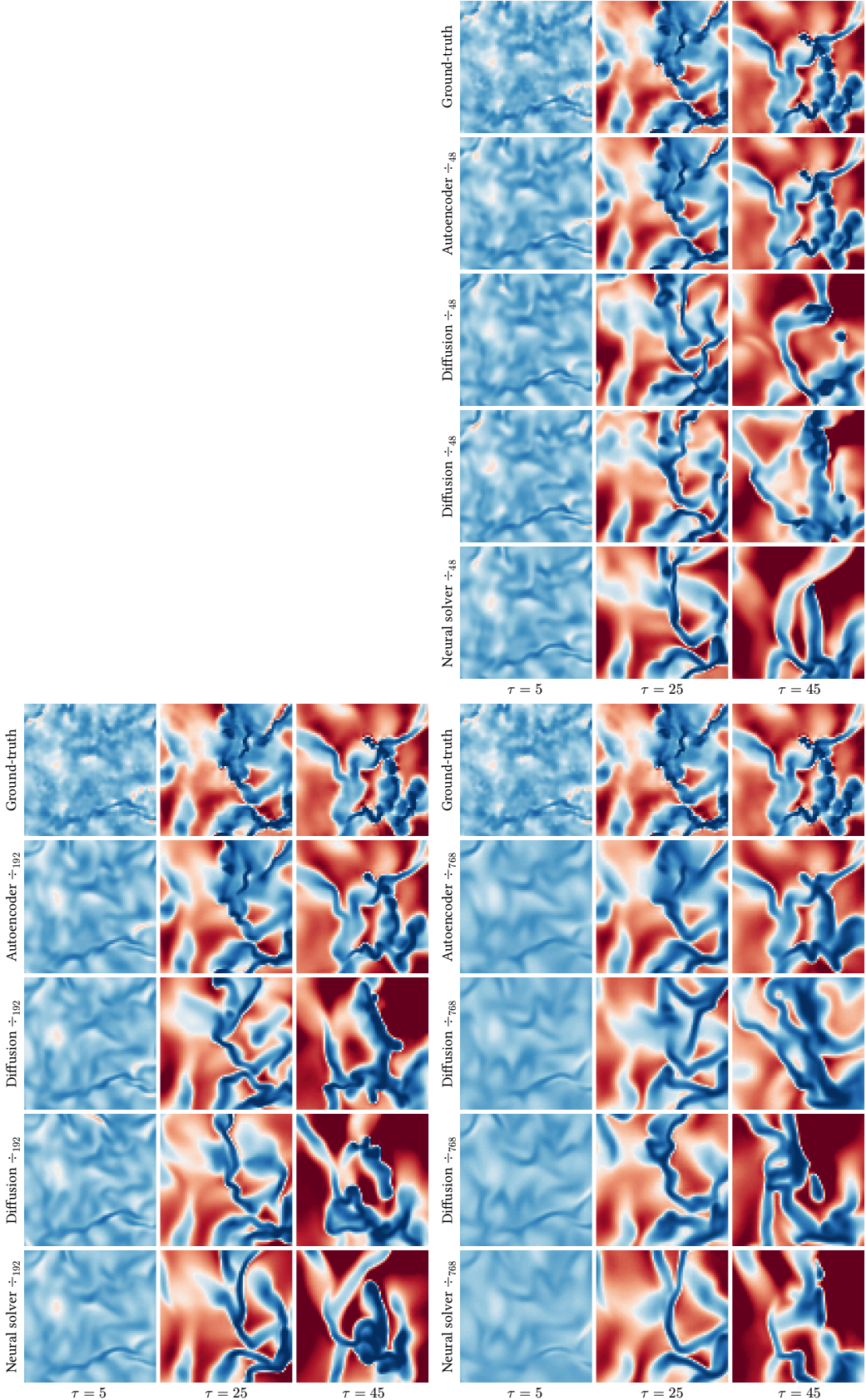


Figure 19. Examples of emulation at different compression rates ( $\div$ ) for the TGC dataset. In this simulation, the initial density is medium and the initial temperature is high ( $\rho_0 = 4.45$ ,  $T_0 = 1000.0$ ).

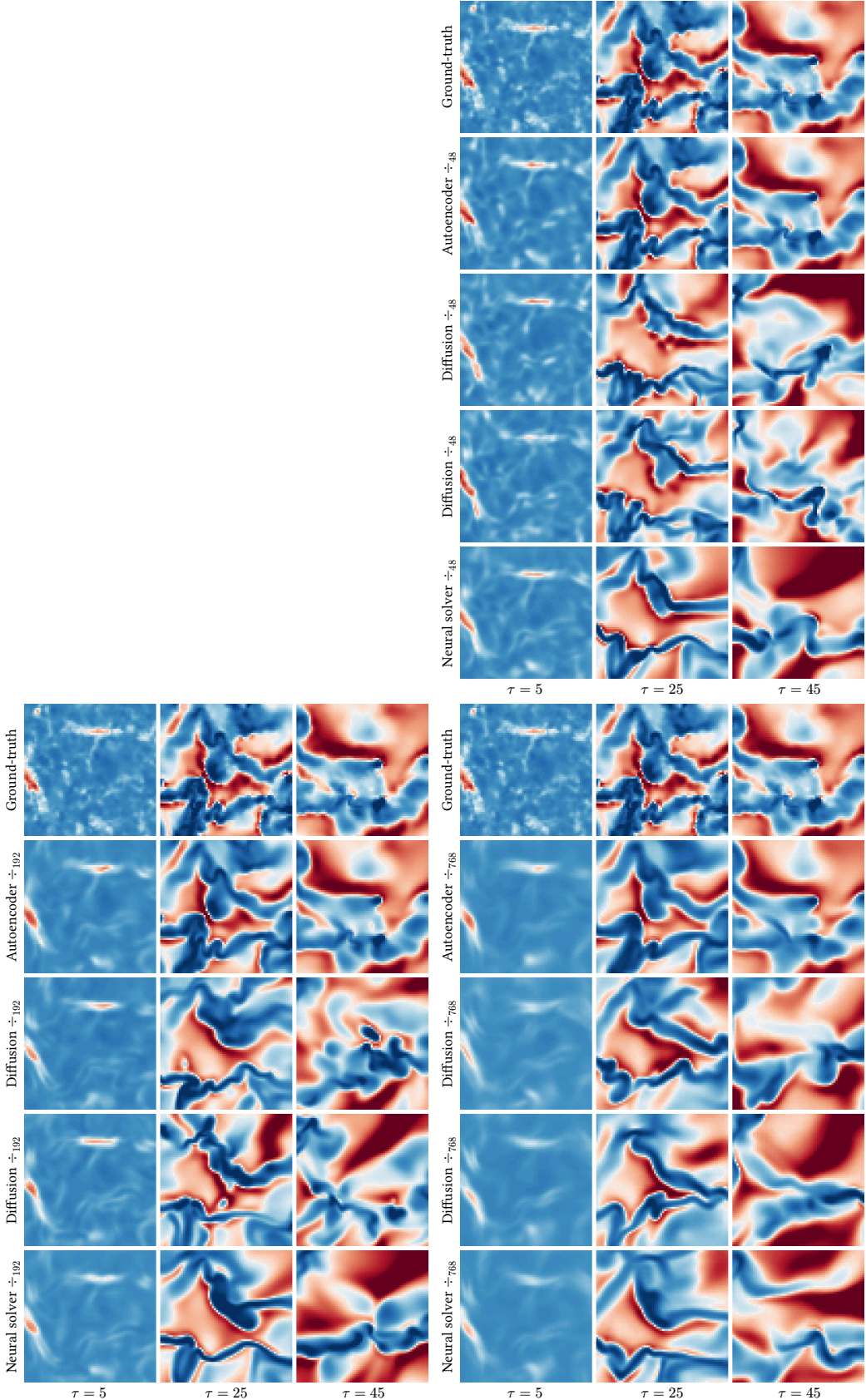


Figure 20. Examples of emulation at different compression rates ( $\div$ ) for the TGC dataset. In this simulation, the initial density is high and the initial temperature is low ( $\rho_0 = 44.5$ ,  $T_0 = 10.0$ ).

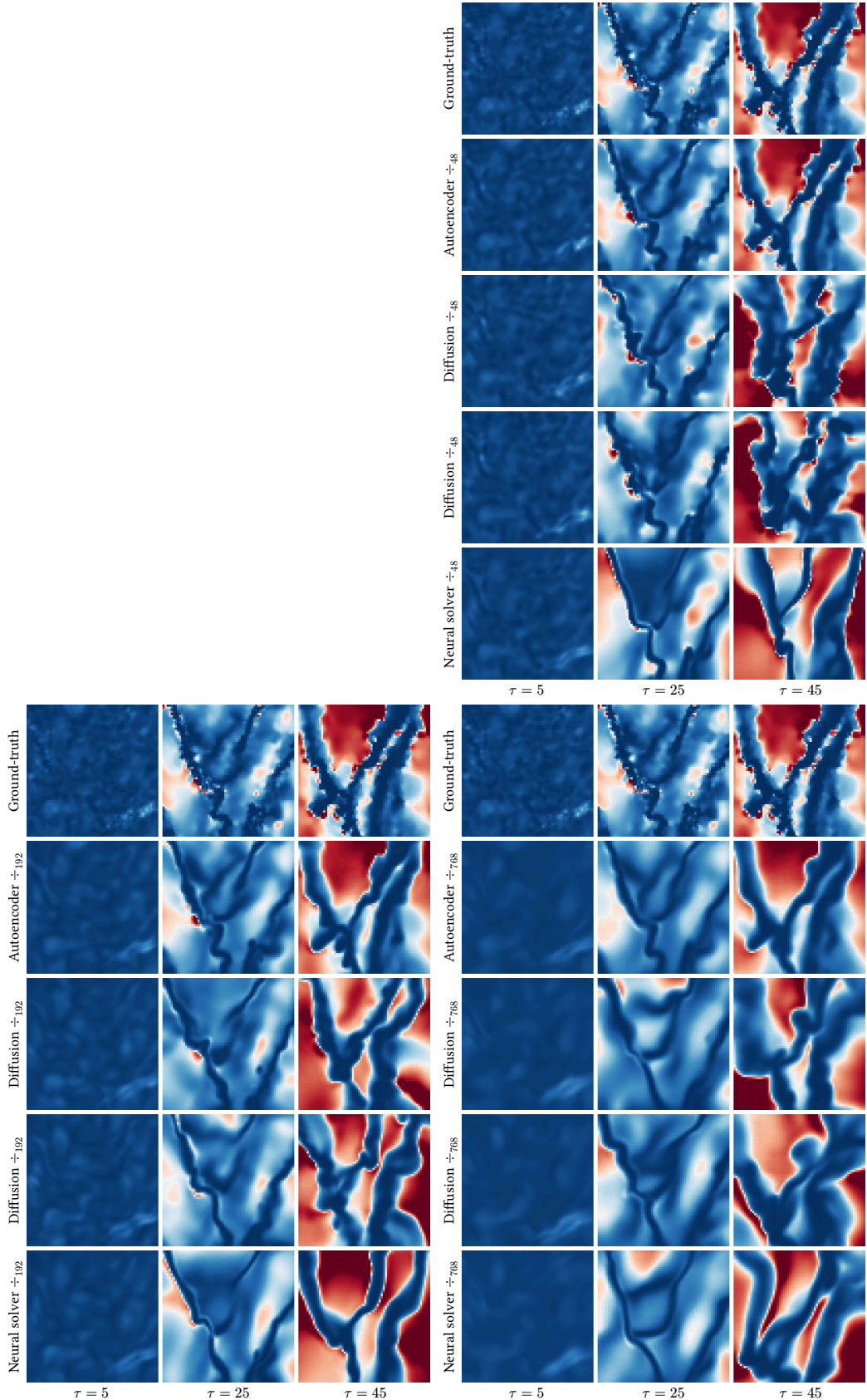


Figure 21. Examples of emulation at different compression rates ( $\div$ ) for the TGC dataset. In this simulation, the initial density is high and the initial temperature is medium ( $\rho_0 = 44.5$ ,  $T_0 = 100.0$ ).

## D Latent space analysis

In this section, we conduct a short analysis of the learned latent representations. We are notably interested in the separability of the latent representation with respect to different parameters  $\theta$ .

For our first experiment, we select a random initial state  $x^1$  from the test split of the Euler dataset. We compute the initial state  $z^1 = E_\psi(x^1)$  for the  $\div_{80}$  auto-encoder. For each heat capacity  $\gamma \in \{1.2, 1.3, 1.4, 1.5, 1.6\}$ , we generate one latent trajectory  $z^{1:L}$  with the diffusion-based emulator. Afterwards we compute the Euclidean distance  $\|z_a^i - z_b^i\|_2$  for each pair  $(\gamma_a, \gamma_b)$  of heat capacities. We report the results in Table 15 and represent the trajectories in Figure 22. As expected, trajectories with similar heat capacity  $\gamma$  are close to each other.

For our second experiment, we compute the latent representations  $z^i = E_\psi(x^i) \in \mathbb{R}^{16 \times 4 \times 64}$  of the  $\div_{64}$  auto-encoder for randomly selected states  $x^i$  of the Rayleigh-Bénard dataset. We then train a small multi-layer perceptron (MLP) to predict the simulation parameters  $\theta$  (Rayleigh and Prandtl numbers) from the latent state's central token  $z^i[8, 2] \in \mathbb{R}^{64}$ . We extract the activations of the MLP's last layer and visualize them with t-SNE [120] in Figure 23. We observe that t-SNE [120] continuously separates latent states with respect to their parameters  $\theta$ , indicating that our auto-encoders learn to distinguish between different physics. We further validate this result by computing the pairwise Bures-Wasserstein distances [121] between the distributions of central tokens  $z^i[8, 2]$  for different Rayleigh and Prandtl numbers. The distances, reported in Tables 16 and 17, are anti-correlated with the similarity of simulation parameters  $\theta$ .

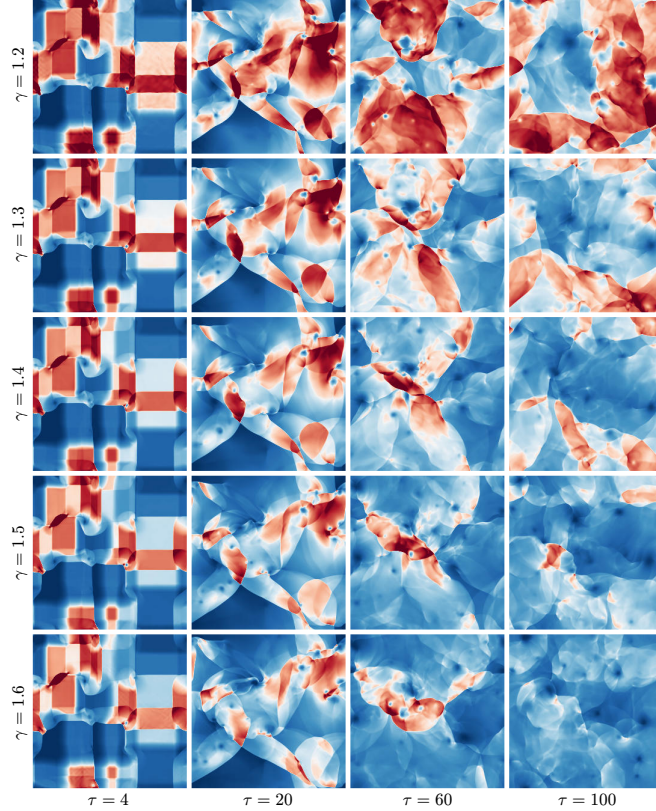


Figure 22. Example of emulated trajectories with different heat capacities  $\gamma \in \{1.2, 1.3, 1.4, 1.5, 1.6\}$  but starting at the same initial state  $x^1$  for the Euler dataset. The energy field is visualized instead of the density field to emphasize the differences.

Table 15. Euclidean distance matrix between emulated trajectories with different heat capacities  $\gamma \in \{1.2, 1.3, 1.4, 1.5, 1.6\}$  but starting at the same initial state  $x^1$  for the Euler dataset.

$\tau = 1$	1.2	1.3	1.4	1.5	1.6	$\tau = 20$	1.2	1.3	1.4	1.5	1.6
1.2	0.00	26.61	32.45	38.46	46.28	1.2	0.00	55.95	64.92	71.06	78.85
1.3	26.61	0.00	14.72	22.09	32.33	1.3	55.95	0.00	38.93	55.03	66.19
1.4	32.45	14.72	0.00	15.26	25.62	1.4	64.92	38.93	0.00	44.00	59.93
1.5	38.46	22.09	15.26	0.00	18.52	1.5	71.06	55.03	44.00	0.00	52.14
1.6	46.28	32.33	25.62	18.52	0.00	1.6	78.85	66.19	59.93	52.14	0.00
$\tau = 60$	1.2	1.3	1.4	1.5	1.6	$\tau = 100$	1.2	1.3	1.4	1.5	1.6
1.2	0.00	74.68	84.37	90.41	96.04	1.2	0.00	74.71	82.09	90.16	94.79
1.3	74.68	0.00	67.06	75.22	82.20	1.3	74.71	0.00	66.72	74.16	81.68
1.4	84.37	67.06	0.00	67.42	76.49	1.4	82.09	66.72	0.00	67.51	74.72
1.5	90.41	75.22	67.42	0.00	71.58	1.5	90.16	74.16	67.51	0.00	69.75
1.6	96.04	82.20	76.49	71.58	0.00	1.6	94.79	81.68	74.72	69.75	0.00

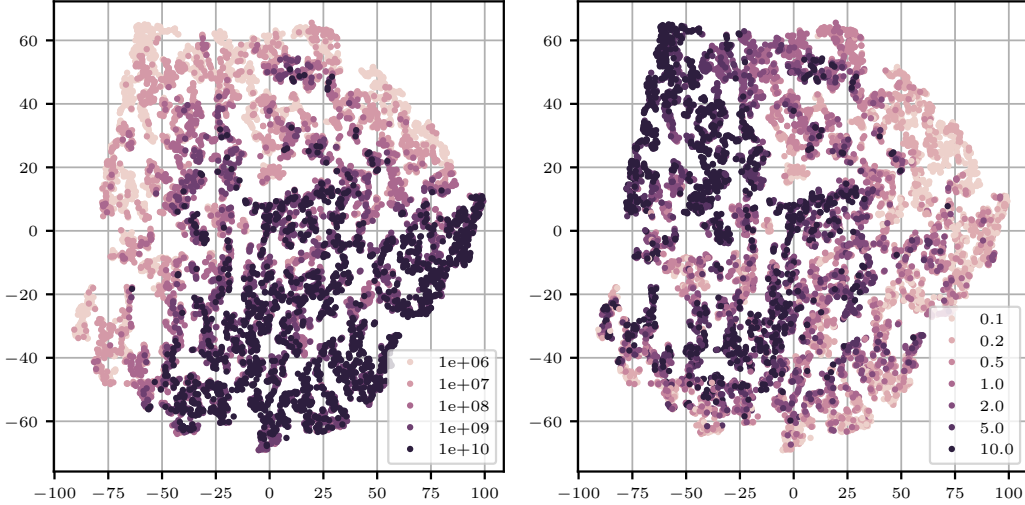


Figure 23. t-SNE [120] visualization of the latent states  $z^i = E_\psi(x^i)$ . The projections are colored with respect to their Rayleigh (left) and Prandtl (right) numbers.

Table 16. Bures-Wasserstein distance matrix between the distributions of latent states  $z^i = E_\psi(x^i)$  with different Rayleigh numbers.

	$10^6$	$10^7$	$10^8$	$10^9$	$10^{10}$
$10^6$	0.000	1.045	1.708	2.279	2.489
$10^7$	1.045	0.000	0.965	1.537	1.794
$10^8$	1.708	0.965	0.000	0.915	1.180
$10^9$	2.279	1.537	0.915	0.000	0.714
$10^{10}$	2.489	1.794	1.180	0.714	0.000

Table 17. Bures-Wasserstein distance matrix between the distributions of latent states  $z^i = E_\psi(x^i)$  with different Prandtl numbers.

	0.1	0.2	0.5	1.0	2.0	5.0	10.0
0.1	0.000	1.367	2.042	2.631	3.244	3.884	4.210
0.2	1.367	0.000	1.269	1.839	2.381	3.007	3.331
0.5	2.042	1.269	0.000	0.986	1.479	2.093	2.398
1.0	2.631	1.839	0.986	0.000	0.930	1.472	1.766
2.0	3.244	2.381	1.479	0.930	0.000	0.988	1.251
5.0	3.884	3.007	2.093	1.472	0.988	0.000	0.711
10.0	4.210	3.331	2.398	1.766	1.251	0.711	0.000